# Precision Measurements and Studies of a Possible Nuclear Dependence of $R = \sigma_L/\sigma_T$

R. Ent, H. Fenker, D. Gaskell (spokesperson), M. Jones, C. Keppel (spokesperson), S. P. Malace (contact and spokesperson), P. Solvignon (spokesperson), B. Sawatzky, and S. Wood
*Thomas Jefferson National Accelerator Facility, Newport News, VA 23606, USA*

A. Accardi, M. E. Christy (spokesperson), J. Diefenbach, Y. Han,
N. Kalantarians, M. Kohl, P. Monaghan, L. Tang, and L. Y. Zhu
*Hampton University, Hampton, VA 23668, USA*

V. Mamyan
*Carnegie Mellon University, Pittsburgh, PA 15213, USA*

W. Boeglin, P. E. C. Markowitz, and J. Reinhold
*Florida International University, Miami, FL 33199, USA*

G. Niculescu and I. Niculescu
*James Madison University, Harrisonburg, VA 22807, USA*

X. Jiang
*Los Alamos National Laboratory, Los Alamos, NM 87544, USA*

V. Sulkosky
*Massachusetts Institute of Technology, Cambridge, MA 02139, USA*

J. Dunne, D. Dutta
*Mississippi State University, Mississippi State, MS 39762, USA*

A. Daniel
*University of Houston, Houston, TX 77004, USA*

A. Atkins, T. Badman, J. Maxwell, S. Phillips, K. Slifer, and R. Zielinski
*University of New Hampshire, Durham, NH 03824, USA*

G. Huber
*University of Regina, Regina, SK S4S0A2, Canada.*

A. Bodek
*University of Rochester, Rochester, NY 14627, USA.*

D. Day, N. Liyanage, O. Rondon, and M. Yurov
*University of Virginia, Charlottesville, VA 22904, USA*

A. Asaturyan, A. Mkrtchyan, H. Mkrtchyan, V. Tadevosyan, and S. Zhamkochyan
*Yerevan Physics Institute, 2 Alikhanyan Brothers St., Yerevan 0036, Armenia*

V. Guzey
*Petersburg Nuclear Physics Institute, St. Petersburg, Russia*

We propose to measure with unprecedented statistical precision inclusive inelastic electron-nucleon and electron-nucleus scattering cross sections in the DIS regime spanning a four-momentum transfer range of $1 < Q^2 < 5\ GeV^2$, and a Bjorken $x$ range of $0.1 < x < 0.6$ for $W^2$ up to 10 GeV using hydrogen, deuterium, beryllium, carbon, copper, silver and gold targets. The cross sections will be used to perform high-precision Rosenbluth separations to extract the ratio $R = \sigma_L/\sigma_T$, $R_A - R_D$, and the transverse $F_1$, longitudinal $F_L$, and $F_2$ structure functions in a model-independent fashion. Recent analyses suggest that $R_A - R_D$ may be different than zero having profound implications for our understanding of the origins of both antishadowing and the nuclear EMC effect. Our proposed measurements would set the most precise limit to date on the possible nuclear modifications of $R$.

## I. BRIEF INTRODUCTION OF FORMALISM

Due to the small value of the electromagnetic coupling constant, the scattering of electrons from nucleons can be well approximated by the exchange of a single virtual photon. In terms of the incident electron energy $E$, the scattered electron energy $E^{'}$, and the scattering angle $\theta$, the absolute value of the exchanged 4-momentum squared $Q^2$ is given by

$$Q^2 = -q^2 = 4EE^{'}\sin^2\frac{\theta}{2} \ . \tag{1}$$

In this one photon exchange approximation, the spin-independent cross section for inclusive electron-nucleon scattering can be expressed in terms of the photon helicity coupling as

$$\frac{d^2\sigma}{d\Omega dE'} = \Gamma\left[\sigma_T(x,Q^2) + \epsilon\sigma_L(x,Q^2)\right] = \Gamma\sigma_T(x,Q^2)\left[1+\epsilon R(x,Q^2)\right] \ , \tag{2}$$

where $\sigma_T$ ($\sigma_L$) is the cross section for photo-absorption of purely transverse (longitudinal) polarized photons. Bjorken $x$ is the fraction of the momentum carried by the quarks and gluons inside the nucleon and can be expressed as $x = \frac{Q^2}{2M(E-E')}$ in the lab frame with nucleon mass $M$. The term $\Gamma$ given by

$$\Gamma = \frac{\alpha E^{'}(W^2 - M^2)}{4\pi^2 Q^2 M E(1-\epsilon)} \tag{3}$$

is the flux of transverse virtual photons expressed in terms of the strong coupling constant $\alpha$, the invariant mass $W$, the energy transfer $\nu = E - E^{'}$, and the virtual photon polarization parameter $\epsilon$:

$$\epsilon = \left[1 + 2(1+\frac{\nu^2}{Q^2})\tan^2\frac{\theta}{2}\right]^{-1} \ . \tag{4}$$

Note that $\epsilon = 0$ for a purely transversely polarized virtual photon. The factor $\epsilon$ can be also expressed in terms of $y = \nu/E$ and $Q^2/E^2$

$$\epsilon = \frac{4(1-y) - \frac{Q^2}{E^2}}{4(1-y) + 2y^2 + \frac{Q^2}{E^2}} \ . \tag{5}$$

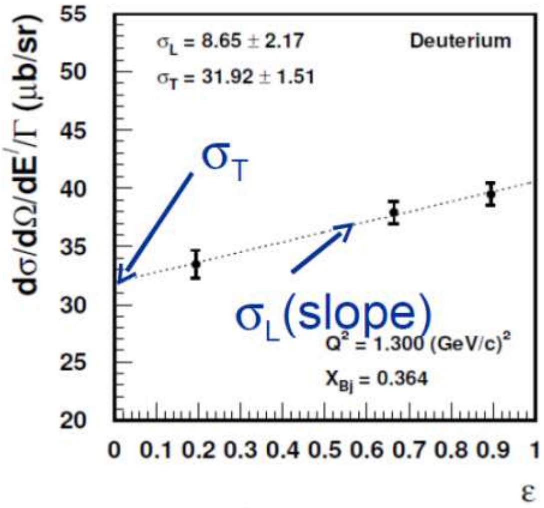

FIG. 1: An example L/T separation on a deuterium target using the Rosenbluth technique.

h

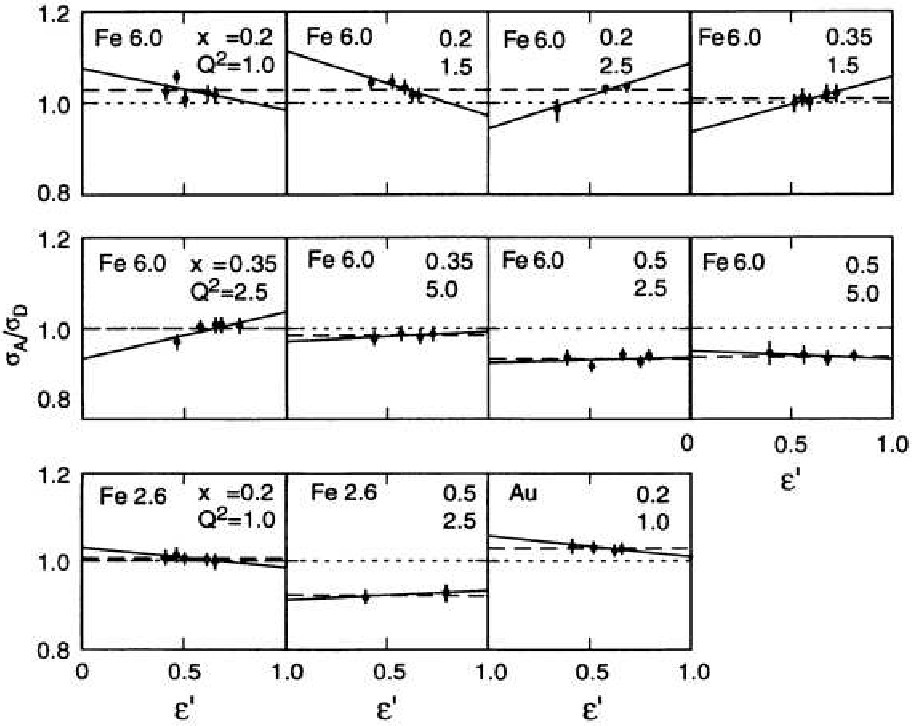

FIG. 2: An example of $R_A - R_D$ extraction on iron and gold targets from the SLAC experiment E140 [1]. Here $\epsilon^{/}$ is defined as $\frac{\epsilon}{(1+\epsilon R_D)}$. Figure taken from [1].

At small $Q^2$ ($<< E^2$), $\epsilon$ only depends on $y$, with the relation $\epsilon = 1 - \frac{y^2}{1+(1-y)^2}$. This implies that $\epsilon = 1$ at $y = 0$, and $\epsilon = 0$ at $y = 1$. The study of the $\epsilon$ dependence at JLab, is therefore complementary to the recent studies of the $\frac{y^2}{1+(1-y)^2}$ dependence at H1 and ZEUS.

In terms of the structure functions $F_1(x,Q^2)$ and $F_2(x,Q^2)$ in the DIS region, the double differential cross section can be written as

$$\frac{d^2\sigma}{d\Omega dE'} = \Gamma \frac{4\pi^2\alpha}{x(W^2 - M^2)} \left[ 2xF_1(x,Q^2) + \epsilon \left( (1 + \frac{4M^2x^2}{Q^2}) F_2(x,Q^2) - 2xF_1(x,Q^2) \right) \right]. \tag{6}$$

A comparison of Equation 2 and Equation 6 shows that $F_1(x,Q^2)$ is purely transverse, while the combination

$$F_L(x,Q^2) = (1 + \frac{4M^2x^2}{Q^2}) F_2(x,Q^2) - 2xF_1(x,Q^2) \tag{7}$$

is purely longitudinal.

The separation of the unpolarized structure functions into longitudinal and transverse parts from cross section measurements can be accomplished via the Rosenbluth technique [2], by making measurements at (at least) two but preferably more $\epsilon$ points at fixed $x$ and $Q^2$. Fitting the reduced cross section, $d\sigma/\Gamma$, linearly in $\epsilon$, yields $\sigma_T$ (and therefore $2xF_1(x,Q^2)$) as the intercept, and $\sigma_L$ (and therefore $F_L(x,Q^2)$) as the slope. The longitudinal to transverse cross section ratio $R(x,Q^2) = \sigma_L/\sigma_T = F_L(x,Q^2)/2xF_1(x,Q^2)$ can then be obtained. An example of this type of extraction is shown in Figure 1 where the inclusive reduced cross section measured on a deuterium target is plotted at fixed $x$ and $Q^2$ as a function of $\epsilon$. The linear fit shown by the dashed line provides $\sigma_L$ as the slope and $\sigma_T$ as the intercept. The fit results are sensitive to the point to point total uncertainty of the reduced cross section, the number of $\epsilon$ points utilized as well as the overall $\epsilon$ range used for fitting. To increase the accuracy of the extraction a very good control of the point-to-point uncertainties is required as well as a wide and detailed coverage in $\epsilon$.

Similarly, the unseparated cross section ratio of nuclear targets to deuterium can be related to the difference in $R$ by

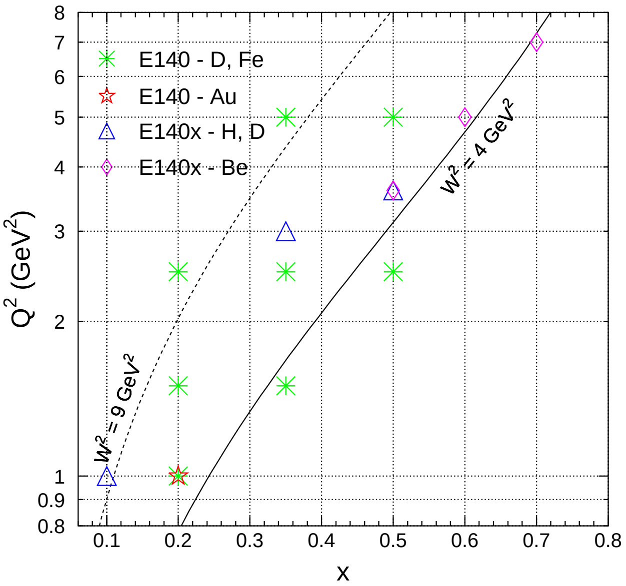

FIG. 3: Kinemtics coverage of available true Rosenbluth LT separations from SLAC [1, 3] (see text).

$$\frac{\sigma_A}{\sigma_D} = \frac{\sigma_A^T}{\sigma_D^T}\left[1 + \frac{\epsilon}{1+\epsilon R_D}(R_A - R_D)\right]. \tag{8}$$

Thus $R_A - R_D$ can be extracted via the Rosenbluth technique by performing a linear fit of the $A/D$ cross section ratios at fixed $x$ and $Q^2$ at different $\epsilon$ settings. An example of such an extraction from the SLAC experiment E140 [1] is shown in Figure 2 where the cross section ratios of gold and iron to deuterium targets are fitted to extract $R_{Au} - R_D$ and $R_{Fe} - R_D$, respectively. Regarding the accuracy of this type of extraction the same reasoning applies as for the measurement of the individual $R$ but in addition a smaller systematic uncertainty is expected for the $R$ difference than for individual $R$ as many of the systematics on the cross sections will cancel in the ratio.

## II. PHYSICS MOTIVATION

### A. Current Status of $R$, $F_L$ and $F_1$ Measurements on Proton and Nuclear Targets

While the nuclear dependence of the inclusive cross section in unpolarized lepton scattering has been measured to good precision (typically a few percent) over a large kinematic region, relatively little is known of the nuclear dependence of the individual structure functions, particularly $F_1$ and $F_L$. In fact, although it is often *assumed* that the nuclear cross section ratio ($\sigma_A/\sigma_D$) is equivalent to the $F_2$ ratio, this is not always a well founded assumption, especially for $\epsilon$ values far from one. As can be seen from Equations 9 and 10, the cross section ratios are only equal to the $F_2$ ratios at all $\epsilon$ if $R_A = R_D$, in which case the nuclear dependence is the same for all the structure functions, $F_2$, $F_1$, and $F_L$. However, such an equivalence is far from established based on the data shown in Figure 4. A determination of the nuclear dependence of the individual structure functions is necessary for a complete understanding of the origin of the EMC effect and of the cross section ratio enhancement in the antishadowing region.

At this point it is worth noting several things in regards to the DIS data shown in Figure 4. First, the uncertainties on most of the individual data for $R_A/R_D$ (or $R_A - R_D$) are typically larger than 30-50% making it difficult to draw firm conclusions. Second, only the SLAC experiments (E140 [1], E140x [3]) performed model independent Rosenbluth separations and their kinematic coverage is hown in Figure 3. The HERMES [4] extractions at low $x$ were performed with a single beam energy, providing no lever arm in $\epsilon$ at fixed $x$ and $Q^2$. The NMC data [5, 6] used multiple beam energies but extracted $R_A - R_D$ using a $Q^2$ dependent fit at fixed $x$. Finally, the SLAC $R_A - R_D$ extractions were performed utilizing cross sections without Coulomb corrections applied. As it will be discussed in a later section, a recent re-extraction of $R_A - R_D$ [7] including the neglected Coulomb corrections, as well as additional data from JLab, hint that $R_A < R_D$ for $Q^2$ of a few GeV and $x$ in the region of the EMC effect. This case is further strenghtened by the *preliminary* data from JLab experiments E04-001, E02-109, and E06-009, which focused on extraction of $R_A - R_D$ and $R_D$ in the **nucleon resonance region** and for $0.1 < Q^2 < 4$ GeV$^2$. The preliminary results for copper in the range $2 < Q^2 < 4$ from the Ph.D. dissertation [8] of V. Mamyan is shown in Figure 5. Final results are expected in the next few months. **The current proposal would extend the existing JLab measurements from the resonance region well into the DIS regime, $W^2$ up to 10 GeV$^2$, covering a significant range in $x$ and $Q^2$ to determine whether the nuclear effects in the EMC and antishadowing regions are the same in $F_1$, $F_2$, and $F_L$.**

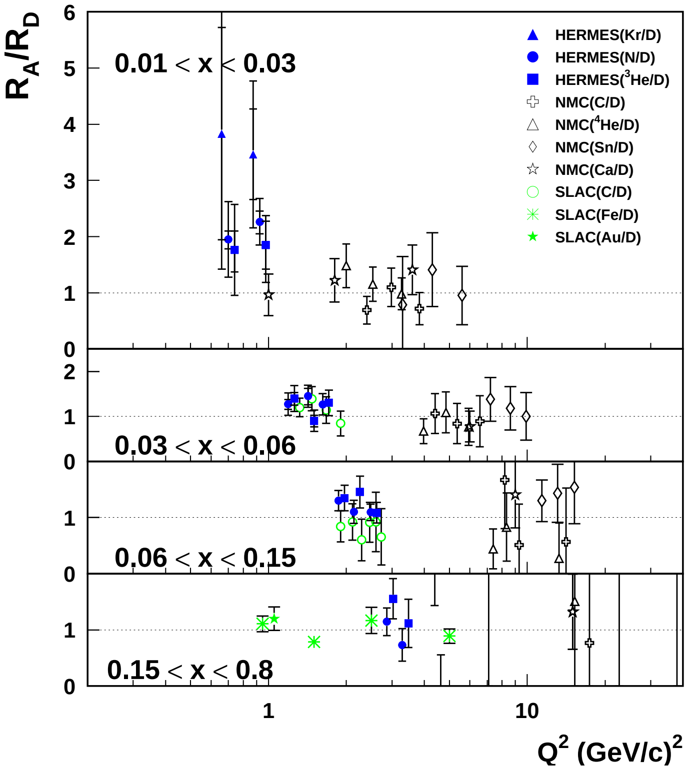

FIG. 4: World data on $R_A/R_D$. Model dependent extractions are included together with the few SLAC data from true Rosenbluth LT separations (see text).

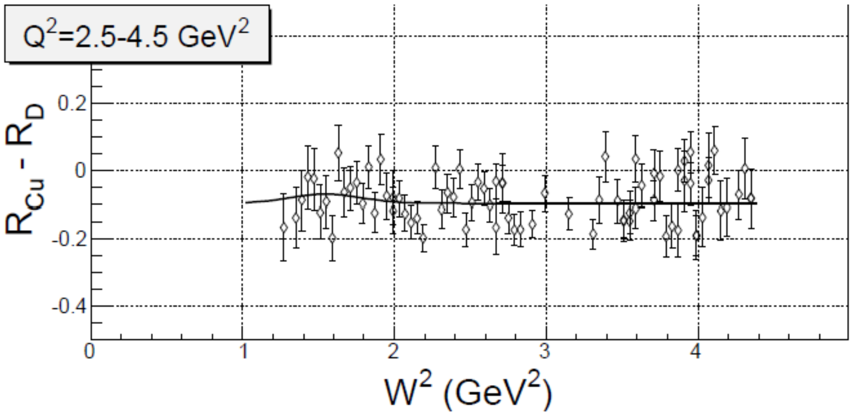

FIG. 5: Preliminary results from Hall C JLab [8] showing that $R_{Cu} < R_D$ in the resonance region.

### B. Implications of a Possible Nuclear Dependence of $R$

Experimentally measured cross section ratios contain both transverse and longitudinal contributions of the structure functions. In terms of the structure function $F_2(x,Q^2)$, one can write the ratio of the nucleus to deuteron photoabsorption cross sections as:

$$\frac{\sigma_A}{\sigma_D} = \frac{F_2^A(x,Q^2)}{F_2^D(x,Q^2)}\frac{1+R_D}{1+R_A}\frac{1+\epsilon R_A}{1+\epsilon R_D} \approx \frac{F_2^A(x,Q^2)}{F_2^D(x,Q^2)}\left[1-\frac{\Delta R(1-\epsilon)}{(1+R_D)(1+\epsilon R_D)}\right], \tag{9}$$

where $A$ refers to the nucleus while $D$ refers to deuteron; $\Delta R$ is the difference between $R_A$ and $R_D$. Similarly one can express the cross section ratios in terms of the $F_1$ structure function ratios according to:

$$\frac{\sigma_A}{\sigma_D} = \frac{F_1^A(x,Q^2)}{F_1^D(x,Q^2)}\frac{1+\epsilon R_A}{1+\epsilon R_D} = \frac{F_1^A(x,Q^2)}{F_1^D(x,Q^2)}\left[1+\frac{\epsilon \Delta R}{(1+\epsilon R_D)}\right]. \tag{10}$$

The cross section ratio $\sigma_A/\sigma_D$ can be identified with the $F_1$ or $F_2$ structure function ratios only under the assumption of trivial nuclear dependence of $R$, i.e. $R_A = R_D$ or in certain kinematic limits. Specifically, $\sigma_A/\sigma_D = F_2^A/F_2^D$ at $\epsilon = 1$ and $\sigma_A/\sigma_D = F_1^A/F_1^D$ at $\epsilon = 0$. In what follows we summarize and discuss studies on implications of a possible nuclear dependence of $R$.

#### 1. *The Antishadowing Region*

The well known behavior of nuclear modifications of the nucleus to deuteron cross section ratio $\sigma_A/\sigma_D$ obtained from electron scattering has the pattern shown in Figure 6, left panel. For small $x$ values, in the *shadowing region*, $x < 0.05 - 0.1$ the ratio is suppressed - the suppression increases with an increasing $A$ and a decrease of $x$. For $0.1 < x < 0.3$, the *antishadowing region*, the ratio is enhanced (few percent effect) with no obvious $A$ dependence. In the interval $0.3 < x < 0.8$ the ratio is suppressed and this is called the *EMC effect*. Finally, for $x > 0.8$ the ratio increases dramatically above unity and this is attributed to the nucleon motion inside the nucleus (Fermi motion). Various models attempt to describe the nuclear modifications of the experimental ratio $\sigma_A/\sigma_D$ but there is no comprehensive understanding of the entire pattern.

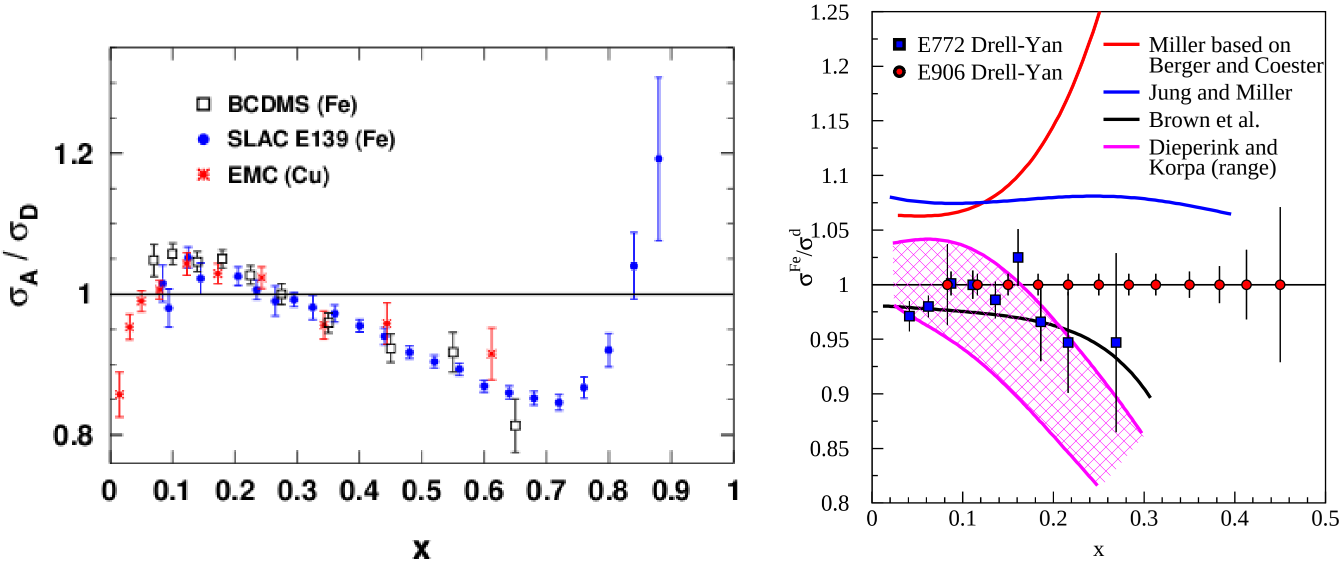

FIG. 6: **Left:** Nuclear modifications of the cross section ratio $\sigma_A/\sigma_D$ as a function of $x$ for iron and copper. The data are from BCDMS [9] (open squares), SLAC E139 [10] (filled circles) and EMC [11] (stars). **Right:** Cross section ratio of iron to deuterium from Drell-Yan experiments E772 [12] (filled squares) and projections from E906 [13] (filled circles) as a function of $x$. The ratio from E772 showed **no** enhancement in the antishadowing region, with limited precision. E906 is underway.

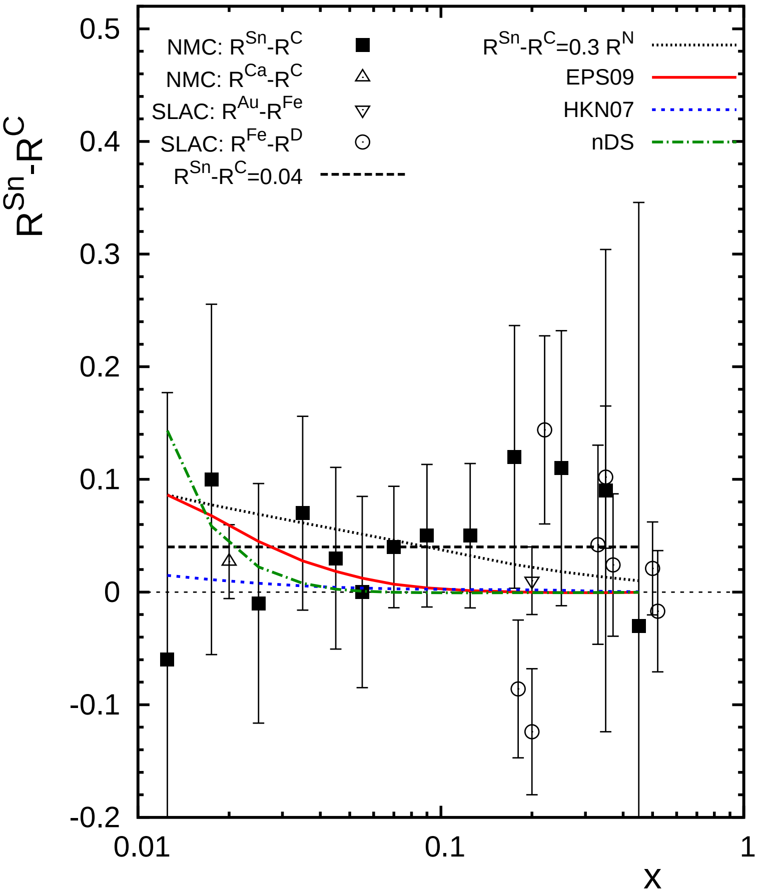

FIG. 7: $R_{Sn} - R_C$ as a function of $x$. Full squares are results of the NMC measurement with the statistical and systematic errors added in quadrature [5]; the long-dash and dotted curves correspond to $R_{Sn} - R_C = 0.04$ and $R_{Sn} - R_C = 0.3R_N$, respectively; the curves labeled $EPS09$, $HKN07$ and $nDS$ correspond to predictions using different nuclear parton distributions. Also shown are the NMC result for $R_{Ca} - R_C$ [6] (triangle), the SLAC result for $R_{Au} - R_{Fe}$ [14] (inverse triangle), and SLAC E140 results for $R_{Fe} - R_D$ as a function of $x$ [1] (open circles). Figure taken from [15].

Unlike the shadowing effect, antishadowing shows little or no sensitivity to $A$ within experimental uncertainties, for example, in the SLAC E139 [10] and NMC data [6]. While antishadowing is observed in nuclear DIS, the cross section enhancement is not seen in nuclear Drell-Yan rates [12] as presented in Figure 6, right panel, nor in the total neutrino-nucleus cross sections for $x > 0.1$ [16]. The deviation of $\sigma_A/\sigma_D$ from unity in this region is of the order of a few percent and most measurements quote normalization uncertainties on the order of 1-2% so it is difficult to quantify the absolute size of the antishadowing effect precisely. From the theory perspective, in the leading twist formalism, the small enhancement of the cross section ratio in the antishadowing region translates into an enhancement of the valence quark and possibly gluon distributions in nuclei in this region [17, 18]. But the pattern and especially the magnitude of nuclear modifications of the gluon distribution in nuclei are very poorly constrained by present data.

A recent study by V. Guzey *et al.* [15] set to examine the impact of the nuclear dependence of $R$, on the extraction of the nucleus to deuteron structure function ratios, $F_2^A/F_2^D$ and $F_1^A/F_1^D$ from $\sigma_A/\sigma_D$ data. Guzey and collaborators demonstrated that in the presence of a small but non-zero difference between $R$ for nuclei and nucleon, the nuclear enhancement in the ratio of the transverse structure functions $F_1^A/F_1^D$ becomes significantly reduced (or even disappears in some cases), indicating that antishadowing is dominated by the longitudinal contribution.

The study used a compilation of measurements of the nuclear dependence of $R$ as shown in Figure 7. It was pointed out in their study that the nuclear dependence of $R$ has not yet being systematically measured so two assumptions for $\Delta R$ would be explored: (absolute) $\Delta R = R_A - R_D = 0.04$ and (relative) $(R_A - R_D)/R_N = 30\%$. The first assumption was based on the NMC measurements of $R_{Sn} - R_C$ at an average $Q^2$ of 10 GeV$^2$ (Figure 7). The second assumption was possible in view of the fact that the NMC $Sn/C$ data allows for a 22 to 120% relative deviation of $\Delta R/R_N$ because of the large uncertainties. It was effectively assumed that $R_A - R_D = R_{Sn} - R_C$ which corresponds

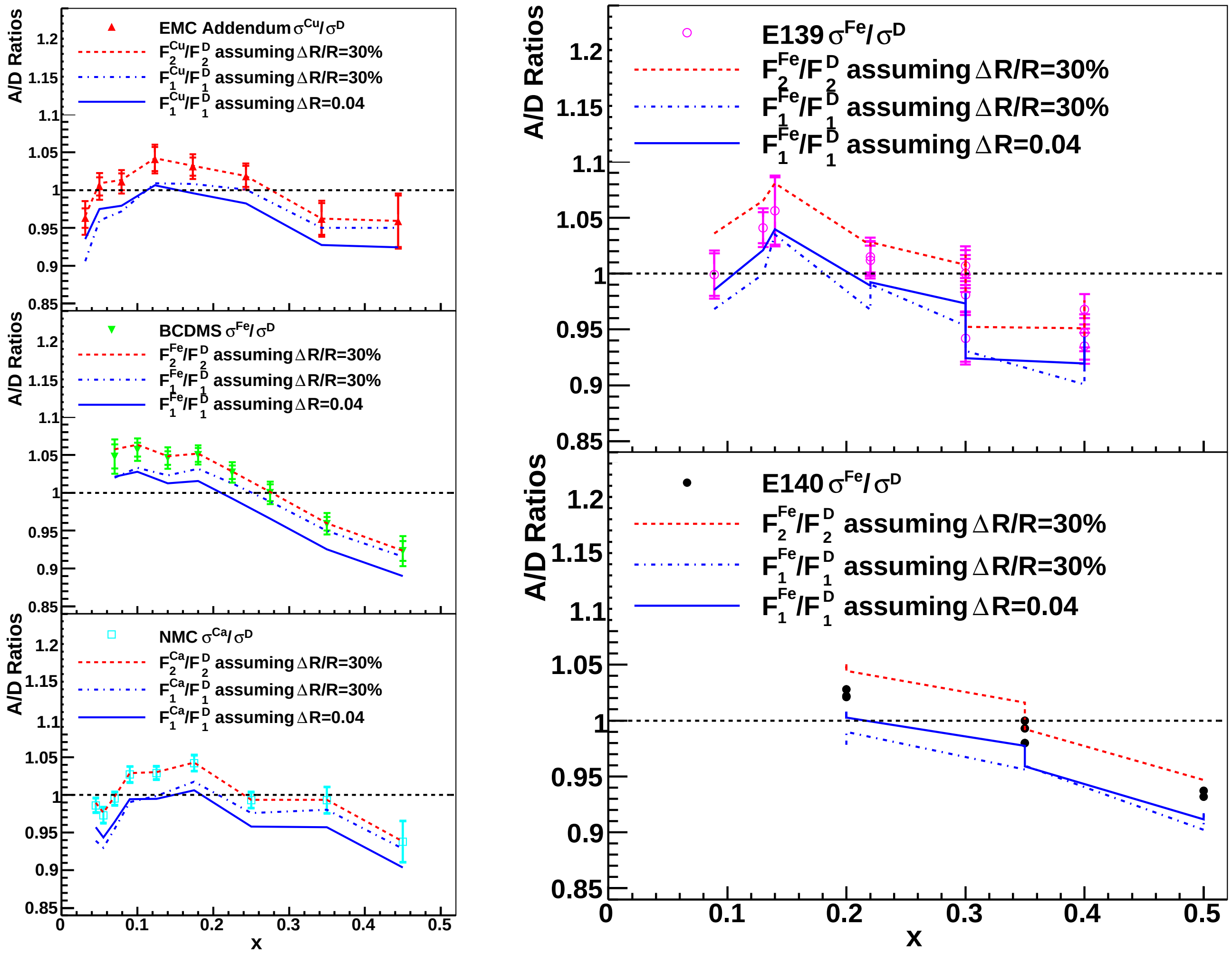

FIG. 8: **Left:** The impact of the nontrivial nuclear dependence of $R$ on the structure function ratios around the antishadowing region for BCDMS $Fe/D$ [9], EMC $Cu/D$ [11] and NMC $Ca/D$ [6] data. The values of $\epsilon$ are close to unity. **Right:** Similar study on SLAC E139 [10] and E140 [1] iron to deuterium data. Figures taken from [15].

to the lower limit for $\Delta R$.

Taken from their study, the impact of these assumptions on selected nuclear DIS data is presented in Figure 8. The low $x$ and high $x$ data points have been neglected the focus being on the antishadowing region. The BCDMS $Fe/D$, EMC $Cu/D$ and NMC $Ca/D$ data shown in Figure 8, left panel, correspond to $\epsilon$ close to unity. So regardless of the assumption for $\Delta R$, one expects that $F_2^A/F_2^D \approx \sigma_A/\sigma_D$ with a very good accuracy. On the other hand, $F_1^A/F_1^D$ is clearly smaller than $\sigma_A/\sigma_D$. Thus, the few percent enhancement of the cross section ratio in the antishadowing region may be reduced or removed altogether for the ratio of the transverse structure functions $F_1^A/F_1^D$.

For the SLAC E139 and E140 $Fe/D$ data presented in Figure 8, right panel, the values of $Q^2$ are rather small and the assumptions for the nuclear dependence of $R$ motivated by the NMC $Sn/C$ measurement at higher $Q^2$ require a significant extrapolation in $Q^2$. Since the values of $\epsilon$ for these two data sets are not close to unity $\Delta R > 0$ leads to noticeable differences between the ratio of the structure functions and the ratio of the cross sections according to the trend described by Equations 9, 10: $F_1^A/F_1^D < \sigma_A/\sigma_D < F_2^A/F_2^D$. Thus the assumed nontrivial nuclear dependence of $R$ leads to a decrease or to a complete disappearance (in some case) of enhancement of the $F_1^A/F_1^D$ structure function ratio in the $0.1 < x < 0.3$ region.

This recently published study highlighted the lack of precision measurements of $R_A - R_D$ and showed that even a small difference in $R_A - R_D$ within the large uncertainties of the available data could have a big impact on the interpretation of the cross section ratio enhancement in the antishadowing region. If confirmed by precision experiments, this observation would indicate that the effect of antishadowing in the cross section ratio is predominantly due to the contribution of the longitudinal structure function $F_L$, instead of $F_1$ as implicitly assumed in most phenomenological analyses and global nuclear parton distribution fits.

### *2. The EMC Effect Region*

At $x > 0.3$, one is exploring the canonical "EMC Effect" region where there is an apparent and well-explored suppression of the inclusive electron scattering cross section from a nucleus. As noted earlier, in most measurements of the EMC effect, it assumed that the cross section ratio is immediately identifiable with the ratio of structure functions, i.e., $\sigma_A/\sigma_D = F_2^A/F_2^D$. This identification of course presumes no (or small) nuclear dependence of $R$ for values of $\epsilon < 1.0$.

The assumption that $R_A = R_D$ at large $x$ has been investigated (see Fig. 4) and no evidence for a significant nuclear dependence of $R$ has been seen in published measurements to date. However, a couple of comments are in order. First, the bulk of the data shown in the bottom panel of Fig. 4 is for $x \leq 0.35$. Second, as noted earlier, only the SLAC E140 experiment performed a true Rosenbluth separation. Other measurements (HERMES and NMC) performed fits at multiple values of $\epsilon$, but not necessarily at fixed $Q^2$, so assumptions had to be made regarding the $Q^2$ dependence of both the structure function ratios and the nuclear dependence of $R$. The most precise measurements relevant to the "EMC region" come from SLAC E140, at $x = 0.5$.

Recently, the SLAC E140 results have been re-analyzed including the effects of the acceleration (deceleration) of the incident (scattered) electron in the Coulomb field from the extra $Z - 1$ protons of the nuclear target [7]. The $\epsilon$ dependence of the $\sigma_A/\sigma_D$ ratios is shown in Fig. 9 for the re-analyzed SLAC E140 data (iron target) at $x = 0.5$ and $Q^2 = 5$ GeV$^2$. In addition, data from SLAC E139 and preliminary copper data from JLab E03103 has been included in the fit. Where the original E140 results yielded a value of $R_A - R_D$ consistent with zero ($-0.017 \pm\ 0.054$), the updated combined fit yields a result of $R_A - R_D = -0.084 \pm 0.045$, clearly implying a non-trivial nuclear dependence of $R$ at large $x$. It is worth noting that both the sign and the magnitude of $R_A - R_D$ from this analysis is consistent with the preliminary results shown in Figure 5.

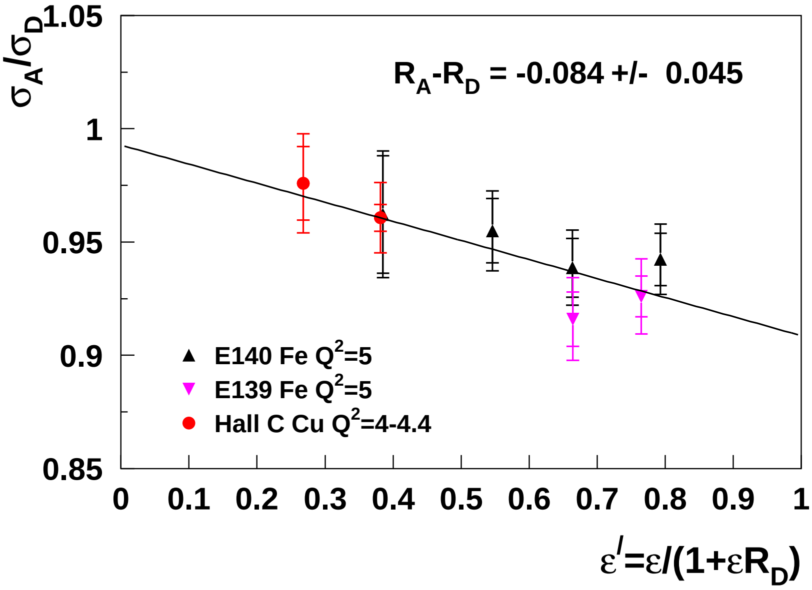

FIG. 9: $\sigma_A/\sigma_D$ vs. $\epsilon' = \epsilon/(1 + \epsilon R_D)$ at $x = 0.5$, $Q^2 = 4 - 5$ GeV$^2$ for iron and copper ratios from SLAC E140 [1], E139 [10], and JLab E03103. The slope of the fitted line directly corresponds to $R_A - R_D$, while the intercept yields $\sigma_T^A/\sigma_T^D = F_1^A/F_1^D$.

The potential consequences of the above result are difficult to overstate. The presumption for the last 30 years has been that the nuclear dependence of the cross section ratios measured in inclusive lepton scattering experiments correspond directly to modifications of the quark distribution functions. In the case of a non–zero $R_A - R_D$ the situation is significantly more complicated. As seen in Fig.9, the fit-intercept, which corresponds to $F_1^A/F_1^D$ is nearly 1.0 at $x = 0.5$. If $F_1$ displays little or no nuclear dependence at this large value of $x$, the implication is that the observed cross section modification comes almost entirely from the longitudinal contribution to the cross section (since $F_1^A/F_1^D = \sigma_T^A/\sigma_T^D$.) Such a conclusion opens the door to very different models of the origin of the EMC effect, including contributions from spin-0 constituents. It is naturally premature to draw such significant conclusions from this re–analysis, however it is clear that the questions raised are significant enough that a larger, more precise data set is urgently needed.

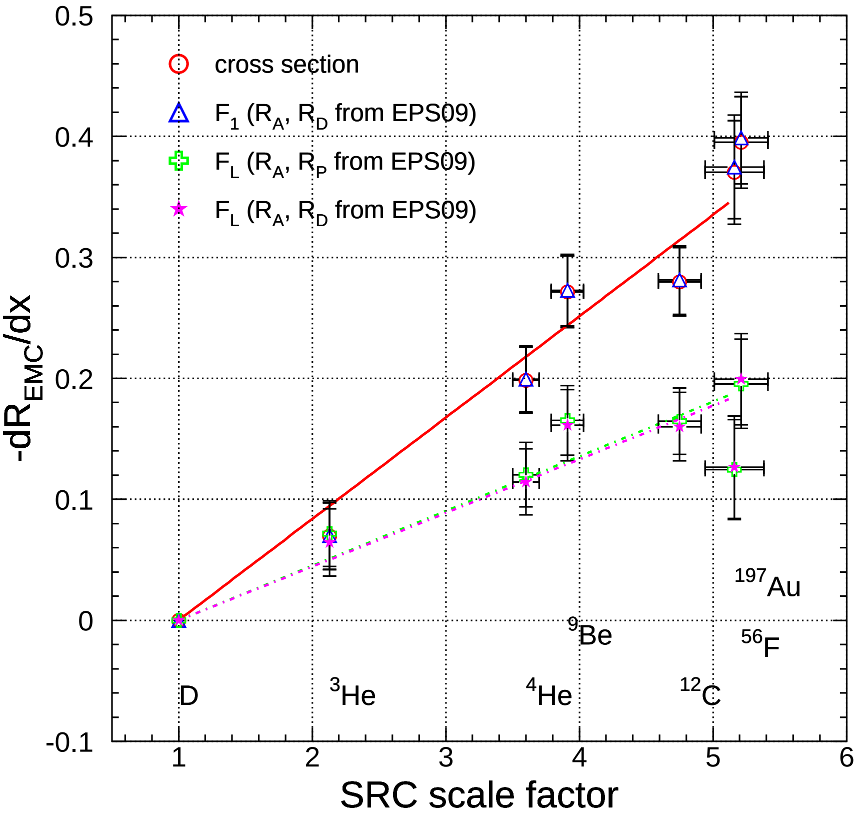

FIG. 10: Size of the EMC Effect, defined as the slope of the ratio, $-dR/dx$, between $x = 0.3$ and $x = 0.7$ vs. the SRC scale factor, $a_2 = \sigma_A/\sigma_D$ for $x > 1.4$. Red open circles show the slopes extracted from the usual EMC ratios (ratio of cross sections), while the blue triangles and magenta stars show the ratios of $F_1$ and $F_L$ extracted from the cross section ratios using values of $R_A$ and $R_D$ from [18]. The green crosses are $F_L$ extracted using $R_p$ instead of $R_D$ from [18].

Recently, significant insight into possible origins of the EMC effect has been obtained through comparisons of the slope of the EMC ratio $dR/dx$ between $0.3 < x < 0.7$ compared to the ratio $a_2 = \sigma_A/\sigma_D$ in the region $x > 1$ [19–21]. The ratio $a_2$ is sensitive to the relative number of short-range correlations (SRCs) in a nucleus, another quantity of much interest in its own right. The comparison of the size of the EMC effect to the number of short range correlations in a nucleus is illustrated in Fig. 10 where the EMC slope is plotted vs. the SRC scale factor ($a_2$). A significant conclusion from studies comparing the two effects is that the EMC effect and Short Range Correlations either stem from some common (as yet unknown) origin or that the SRC ratio serves an effective measurement of some quantity like nucleon virtuality or local density experienced by a nucleon participating in a correlated pair, which in turn gives rise to the EMC effect. These conclusions are drawn from the fact that the correlation between the two observables is quite robust, and that both even measure the same relative effect for a nucleus like beryllium, which has a relatively small average density, but whose EMC effect is more comparable to a nucleus with a higher average density like carbon [22].

However, once once considers the possibility that $R$ is an $A$-dependent quantity, the interpretation becomes more complicated. If the EMC effect and SRCs exhibit such an excellent correlation, but the size of the EMC effect is in part coming from contributions from longitudinal photons, what does this imply about the underlying cause of either, or both? Is the view that both stem from a common origin still tenable?

In addition to the more commonly plotted target ratios, Fig. 10 also shows the EMC effect slope one would extract for the $F_1$ and $F_L$ structure functions, using the EPS09 fit for $R_A$ and $R_D$ [18]. Even when constrained by the existing world data (which one should recall is rather sparse at large $x$), one can see a significant difference between the size of the ratio slopes between the two structure functions. Yet, interestingly, the correlation between the EMC slope and the SRC scale factor is quite good for either quantity.

As shown above, studies of the EMC effect are approaching sufficient quantitative precision that the current experimental situation regarding the nuclear dependence of $R$ is wholly unacceptable. While earlier measurements had suggested that $R_A - R_D$ was small or zero, the more recent re-analysis suggests this may not be the case. The recently observed connection between the EMC effect and Short Range Correlations is very exciting, but the interpretation must remain somewhat ambiguous until it is established whether this connection applies in the same way to all components $(F_1, F_2, F_L)$ of the inclusive cross section.

## III. PROPOSED MEASUREMENTS

We propose to measure with unprecedented statistical precision inclusive inelastic electron-nucleon and electron-nucleus scattering cross sections in the DIS regime ($x$ from 0.1 to 0.6 and $Q^2$ from 1 to 5 GeV$^2$) on hydrogen, deuterium, beryllium, carbon, copper silver and gold targets to extract $R_A$, $R_A - R_D$, $F_L$, $F_1$ and $F_2$ in an model independent fashion. We will use the well suited standard Hall C 12 GeV equipment, the High Momentum Spectrometer (HMS) and the Super-High Momentum Spectrometer (SHMS). We will use 4 cm cryogenic hydrogen and deuterium targets as well as 2% radiation length (r.l.) solid targets beryllium, carbon, copper, silver and gold. An aluminum target will only be used to measure background coming from the walls of the hydrogen and deuterium targets. To achieve the best possible precision for our measurements of $\sigma_L$ and $\sigma_T$, 6 beam energies are required: 4.4, 5.5, 6.6, 7.7, 8.8 and 11 GeV (two of these non-standard beam eneries). Given the superior figure of merit of JLab the improvement in the statistical precision will be up to a factor of 4 when compared to SLAC E140 [1].

In what follows we detail the choice of kinematics, we present the physics rates calculations and estimates of expected backgrounds and corrections to the proposed cross sections. We outline the beam-time estimates needed to achieve the desired statistical precision and we discuss the impact of our proposed measurements.

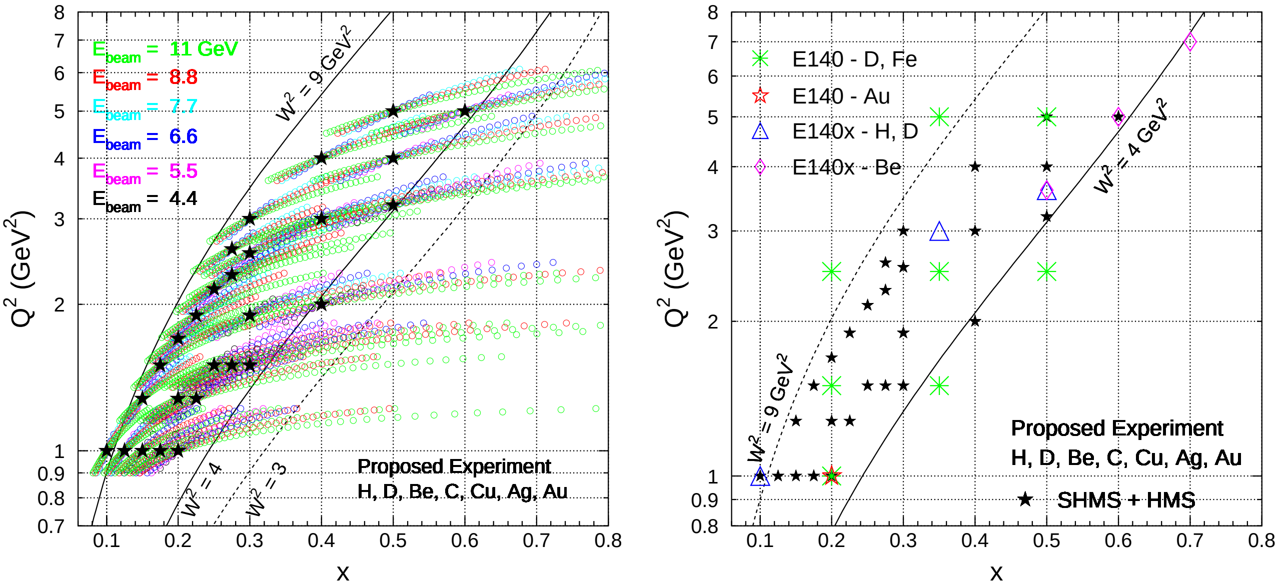

FIG. 11: **Left:** Proposed central kinematics shown in black stars together with the coverage given by the momentum acceptance of the Hall C spectrometers HMS and SHMS indicated by empty circles on a $Q^2$ vs $x$ grid. The angular acceptance of the spectrometers is not shown here as we plan to extract the cross sections at fixed central angle by averaging over the angular acceptance after kinematic corrections. The solid and dotted curves indicate the $W^2$ coverage our focus being roughly on the region of $W^2$ from 3 to 9 GeV$^2$. **Right:** Our proposed central kinematic coverage compared to that of the SLAC experiments E140 [1] and E140x [3]. The statistical uncertainty for the SLAC experiments varies between 0.6% and 2.2% while we aim to achieve a statistical precision of 0.2% to 0.5%.

| $x$ | $Q^2$ | $E_B$ | $E_p$ | $\theta$ | $\epsilon$ |
|---|---|---|---|---|---|
| 0.100 | 1 | 6.6 | 1.271 | 19.881 | 0.356 |
| 0.100 | 1 | 7.7 | 2.371 | 13.440 | 0.551 |
| 0.100 | 1 | 8.8 | 3.471 | 10.381 | 0.673 |
| 0.100 | 1 | 11 | 5.671 | 7.259 | 0.809 |
| 0.125 | 1 | 5.5 | 1.237 | 22.104 | 0.406 |
| 0.125 | 1 | 6.6 | 2.337 | 14.629 | 0.613 |
| 0.125 | 1 | 7.7 | 3.437 | 11.155 | 0.732 |
| 0.125 | 1 | 8.8 | 4.537 | 9.077 | 0.805 |
| 0.125 | 1 | 11 | 6.736 | 6.659 | 0.885 |
| 0.150 | 1 | 4.4 | 0.847 | 30.015 | 0.338 |
| 0.150 | 1 | 6.6 | 3.047 | 12.802 | 0.745 |
| 0.150 | 1 | 8.8 | 5.247 | 8.439 | 0.871 |
| 0.150 | 1 | 11 | 7.447 | 6.333 | 0.923 |
| 0.150 | 1.28 | 5.5 | 0.953 | 28.616 | 0.309 |
| 0.150 | 1.28 | 6.6 | 2.053 | 17.682 | 0.546 |
| 0.150 | 1.28 | 7.7 | 3.153 | 13.186 | 0.686 |
| 0.150 | 1.28 | 8.8 | 4.253 | 10.612 | 0.772 |
| 0.150 | 1.28 | 11 | 6.453 | 7.699 | 0.865 |
| 0.175 | 1 | 4.4 | 1.355 | 23.633 | 0.526 |
| 0.175 | 1 | 5.5 | 2.455 | 15.641 | 0.721 |
| 0.175 | 1 | 6.6 | 3.555 | 11.849 | 0.819 |
| 0.175 | 1 | 8.8 | 5.755 | 8.058 | 0.907 |
| 0.175 | 1 | 11 | 7.955 | 6.128 | 0.944 |
| 0.175 | 1.5 | 5.5 | 0.932 | 31.379 | 0.298 |
| 0.175 | 1.5 | 6.6 | 2.032 | 19.250 | 0.538 |
| 0.175 | 1.5 | 7.7 | 3.132 | 14.326 | 0.679 |
| 0.175 | 1.5 | 8.8 | 4.232 | 11.518 | 0.767 |
| 0.175 | 1.5 | 11 | 6.432 | 8.349 | 0.863 |
| 0.200 | 1 | 4.4 | 1.735 | 20.849 | 0.646 |
| 0.200 | 1 | 5.5 | 2.835 | 14.548 | 0.791 |
| 0.200 | 1 | 6.6 | 3.935 | 11.260 | 0.864 |
| 0.200 | 1 | 8.8 | 6.135 | 7.803 | 0.930 |
| 0.200 | 1 | 11 | 8.335 | 5.986 | 0.957 |
| 0.200 | 1.28 | 4.4 | 0.989 | 31.461 | 0.384 |
| 0.200 | 1.28 | 6.6 | 3.189 | 14.164 | 0.762 |
| 0.200 | 1.28 | 8.8 | 5.389 | 9.423 | 0.879 |
| 0.200 | 1.28 | 11 | 7.589 | 7.099 | 0.928 |
| 0.200 | 1.7 | 5.5 | 0.970 | 32.782 | 0.307 |
| 0.200 | 1.7 | 6.6 | 2.070 | 20.315 | 0.544 |
| 0.200 | 1.7 | 7.7 | 3.170 | 15.164 | 0.683 |
| 0.200 | 1.7 | 8.8 | 4.270 | 12.209 | 0.770 |
| 0.200 | 1.7 | 11 | 6.470 | 8.864 | 0.864 |

TABLE I: Choice of central kinematics to measure the nuclear dependence of $R$. Here the units for four-momentum transferred squared $Q^2$, beam energy $E_B$, scattered electron energy $E_p$, and angle $\theta$ are GeV$^2$, GeV, GeV/$c$ and degrees, respectively. For each fixed ($x$,$Q^2$) *LT* extraction both SHMS and HMS will be used complementary.

| $x$ | $Q^2$ | $E_B$ | $E_p$ | $\theta$ | $\epsilon$ |
|---|---|---|---|---|---|
| 0.225 | 1.28 | 4.4 | 1.368 | 26.657 | 0.521 |
| 0.225 | 1.28 | 5.5 | 2.468 | 17.663 | 0.717 |
| 0.225 | 1.28 | 6.6 | 3.568 | 13.388 | 0.816 |
| 0.225 | 1.28 | 8.8 | 5.768 | 9.108 | 0.906 |
| 0.225 | 1.28 | 11 | 7.968 | 6.928 | 0.943 |
| 0.225 | 1.9 | 5.5 | 1.000 | 34.180 | 0.312 |
| 0.225 | 1.9 | 6.6 | 2.100 | 21.337 | 0.547 |
| 0.225 | 1.9 | 7.7 | 3.200 | 15.962 | 0.686 |
| 0.225 | 1.9 | 8.8 | 4.300 | 12.866 | 0.771 |
| 0.225 | 1.9 | 11 | 6.500 | 9.350 | 0.865 |
| 0.250 | 1.5 | 4.4 | 1.203 | 30.877 | 0.456 |
| 0.250 | 1.5 | 5.5 | 2.303 | 19.817 | 0.677 |
| 0.250 | 1.5 | 6.6 | 3.403 | 14.849 | 0.790 |
| 0.250 | 1.5 | 8.8 | 5.603 | 10.006 | 0.893 |
| 0.250 | 1.5 | 11 | 7.803 | 7.580 | 0.936 |
| 0.250 | 2.15 | 5.5 | 0.917 | 38.105 | 0.280 |
| 0.250 | 2.15 | 6.6 | 2.017 | 23.183 | 0.525 |
| 0.250 | 2.15 | 7.7 | 3.117 | 17.213 | 0.670 |
| 0.250 | 2.15 | 8.8 | 4.217 | 13.824 | 0.759 |
| 0.250 | 2.15 | 11 | 6.417 | 10.012 | 0.858 |
| 0.275 | 1.5 | 4.4 | 1.493 | 27.643 | 0.555 |
| 0.275 | 1.5 | 5.5 | 2.593 | 18.663 | 0.736 |
| 0.275 | 1.5 | 6.6 | 3.693 | 14.250 | 0.828 |
| 0.275 | 1.5 | 8.8 | 5.893 | 9.756 | 0.912 |
| 0.275 | 1.5 | 11 | 8.093 | 7.442 | 0.947 |
| 0.275 | 1.3 | 5.5 | 1.043 | 36.913 | 0.318 |
| 0.275 | 1.3 | 6.6 | 2.143 | 23.264 | 0.550 |
| 0.275 | 1.3 | 7.7 | 3.243 | 17.456 | 0.688 |
| 0.275 | 1.3 | 8.8 | 4.343 | 14.091 | 0.772 |
| 0.275 | 1.3 | 11 | 6.543 | 10.256 | 0.866 |
| 0.275 | 2.6 | 6.6 | 1.562 | 29.088 | 0.408 |
| 0.275 | 2.6 | 7.7 | 2.662 | 20.516 | 0.586 |
| 0.275 | 2.6 | 8.8 | 3.762 | 16.110 | 0.699 |
| 0.275 | 2.6 | 11 | 5.962 | 11.427 | 0.823 |
| 0.300 | 1.5 | 4.4 | 1.735 | 25.606 | 0.628 |
| 0.300 | 1.5 | 5.5 | 2.835 | 17.841 | 0.780 |
| 0.300 | 1.5 | 6.6 | 3.935 | 13.802 | 0.856 |
| 0.300 | 1.5 | 8.8 | 6.135 | 9.561 | 0.926 |
| 0.300 | 1.5 | 11 | 8.335 | 7.333 | 0.955 |
| 0.300 | 1.9 | 4.4 | 1.025 | 37.874 | 0.378 |
| 0.300 | 1.9 | 5.5 | 2.125 | 23.261 | 0.628 |
| 0.300 | 1.9 | 6.6 | 3.225 | 17.183 | 0.758 |
| 0.300 | 1.9 | 7.7 | 4.325 | 13.718 | 0.832 |
| 0.300 | 1.9 | 8.8 | 5.425 | 11.449 | 0.877 |
| 0.300 | 1.9 | 11 | 7.625 | 8.632 | 0.926 |

TABLE II: Choice of central kinematics to measure the nuclear dependence of $R$ (continuation of Table I). Units are the same as specified in Table I.

| $x$ | $Q^2$ | $E_B$ | $E_p$ | $\theta$ | $\epsilon$ |
|---|---|---|---|---|---|
| 0.300 | 2.55 | 5.5 | 0.970 | 40.438 | 0.289 |
| 0.300 | 2.55 | 6.6 | 2.070 | 24.948 | 0.530 |
| 0.300 | 2.55 | 7.7 | 3.170 | 18.599 | 0.673 |
| 0.300 | 2.55 | 8.8 | 4.270 | 14.968 | 0.762 |
| 0.300 | 2.55 | 11 | 6.470 | 10.861 | 0.859 |
| 0.300 | 3 | 6.6 | 1.271 | 34.795 | 0.327 |
| 0.300 | 3 | 7.7 | 2.371 | 23.388 | 0.527 |
| 0.300 | 3 | 8.8 | 3.471 | 18.030 | 0.655 |
| 0.300 | 3 | 11 | 5.671 | 12.590 | 0.797 |
| 0.400 | 2 | 4.4 | 1.735 | 29.652 | 0.610 |
| 0.400 | 2 | 5.5 | 2.835 | 20.629 | 0.768 |
| 0.400 | 2 | 6.6 | 3.935 | 15.950 | 0.848 |
| 0.400 | 2 | 8.8 | 6.135 | 11.044 | 0.921 |
| 0.400 | 2 | 11 | 8.335 | 8.470 | 0.952 |
| 0.400 | 3 | 5.5 | 1.503 | 35.057 | 0.442 |
| 0.400 | 3 | 6.6 | 2.603 | 24.119 | 0.634 |
| 0.400 | 3 | 7.7 | 3.703 | 18.667 | 0.745 |
| 0.400 | 3 | 8.8 | 4.803 | 15.309 | 0.814 |
| 0.400 | 3 | 11 | 7.003 | 11.325 | 0.889 |
| 0.400 | 4 | 6.6 | 1.271 | 40.395 | 0.313 |
| 0.400 | 4 | 7.7 | 2.371 | 27.069 | 0.516 |
| 0.400 | 4 | 8.8 | 3.471 | 20.848 | 0.646 |
| 0.400 | 4 | 11 | 5.671 | 14.547 | 0.791 |
| 0.500 | 3.2 | 4.4 | 0.989 | 50.765 | 0.324 |
| 0.500 | 3.2 | 5.5 | 2.089 | 30.596 | 0.590 |
| 0.500 | 3.2 | 6.6 | 3.189 | 22.483 | 0.732 |
| 0.500 | 3.2 | 7.7 | 4.289 | 17.907 | 0.813 |
| 0.500 | 3.2 | 8.8 | 5.389 | 14.925 | 0.863 |
| 0.500 | 3.2 | 11 | 7.589 | 11.235 | 0.918 |
| 0.500 | 4 | 5.5 | 1.237 | 45.089 | 0.343 |
| 0.500 | 4 | 6.6 | 2.337 | 29.503 | 0.565 |
| 0.500 | 4 | 7.7 | 3.437 | 22.418 | 0.696 |
| 0.500 | 4 | 8.8 | 4.537 | 18.212 | 0.778 |
| 0.500 | 4 | 11 | 6.737 | 13.342 | 0.868 |
| 0.500 | 5 | 6.6 | 1.271 | 45.413 | 0.299 |
| 0.500 | 5 | 7.7 | 2.371 | 30.337 | 0.504 |
| 0.500 | 5 | 8.8 | 3.471 | 23.342 | 0.637 |
| 0.500 | 5 | 11 | 5.671 | 16.276 | 0.785 |
| 0.600 | 5 | 5.5 | 1.059 | 55.189 | 0.270 |
| 0.600 | 5 | 6.6 | 2.159 | 34.455 | 0.512 |
| 0.600 | 5 | 7.7 | 3.259 | 25.791 | 0.658 |
| 0.600 | 5 | 8.8 | 4.359 | 20.799 | 0.750 |
| 0.600 | 5 | 11 | 6.559 | 15.127 | 0.851 |

TABLE III: Choice of central kinematics to measure the nuclear dependence of $R$ (continuation of Table II). Due to rate limitations the kinematic point of $x = 0.6$ will be covered with deuterium, beryllium, carbon and copper only, silver will be used for $x = 0.1$ - 0.3 and gold for $x = 0.1$ - 0.4.

### A. Kinematics

Our goal is to perform precise $LT$ separations in the kinematic range of $x = 0.1$ to 0.6 covering the antishadowing and the EMC effect regions. Figure 11, left panel, shows our choice of kinematics. The black stars indicate the fixed ($x$ , $Q^2$) settings each leading to one extraction at central kinematics of $R_A$, $R_A - R_D$, $F_1$, $F_L$ and $F_2$. For each fixed ($x$ , $Q^2$) setting we plan at least four and up to six $\epsilon$ points measurements each obtained by using different beam energies and central spectrometers settings in $E_p$ and $\theta$. Details of the kinematic coverage are also shown in Tables I, II and III.

Given the large momentum acceptance of the SHMS (-10% to +22% ) and HMS (±8%) additional $LT$ extractions can be performed using the data collected within the acceptance by applying only small $Q^2$ corrections thus exploiting to the fullest the unique capabilities of the Hall C spectrometers. For a given central kinematic setting defined by $(x, Q^2, E_B, E_p, \theta)$ we bin the momentum acceptance of the spectrometers in intervals corresponding to a size in $W^2$ of 0.1 GeV$^2$ (each such bin is shown as an empty circle in Figure 11). At certain $(x, Q^2)$, the fully desired $\epsilon$-range can only be achieved using both the HMS and the SHMS. We plan to and assume that we can cross-calibrate the two spectrometers to the level of 1% precision. Some of the momentum scans that can be covered with both spectrometers will be measured with both for cross-calibration. Measurements at each of the settings shown in Figure 11, left panel, will be performed on hydrogen, deuterium, beryllium, carbon, copper, silver and gold except for $x = 0.6$ where due to rate limitations only deuterium, beryllium, carbon and copper will be used while the measurements on the silver target will cover only the antishadowing region from $x = 0.1$ to $x = 0.3$.

In Figure 11, right panel, we show the central kinematic coverage of our proposed measurements (black stars) compared to that of the SLAC experiments E140 [1] (stars and snowflakes) and E140x [3] (triangles and diamonds). Experiment E140 measured inclusive cross sections from electron scattering on deuterium, iron and gold targets for Rosenbluth $LT$ separations and extracted $R_{Fe} - R_D$ at $x = 0.2$, 0.35, 0.5 and $R_{Au} - R_D$ at x = 0.2. The number of $\epsilon$ points used per extraction varied between two to five with a the statistical uncertainty at the cross section level between 0.6% and 1.3% for deuterium, 0.6% to 2.2% for iron and 0.6% to 1.4% for gold. The systematic uncertainty varied between 0.5% and 0.7%. Experiment E140x performed $LT$ separations on hydrogen and deuterium targets at $x = 0.1$, 0.35 and 0.5 and on beryllium at $x = 0.5$, 0.6 and 0.7. It extracted $R_{deuterium} - R_{hydrogen}$ at $x$ of 0.1, 0.35 and 0.5 and $R_{beryllium} - R_{hydrogen}$ at $x = 0.5$. The statistical uncertainty on this measurement was around 1% with a systematic of at most 0.8%. With our proposed measurements we plan to drastically reduce the statistical uncertainty aiming for 0.2% to 0.5%.

### B. Physics Rates

We calculated the electron rates for the hydrogen target using the cross section model developed by M.E. Christy [23]. This is an empirical fit to measurements of inclusive inelastic electron-proton cross sections in the kinematic range of four-momentum transfer $0 < Q^2 < 8$ GeV$^2$ and final state invariant mass $1.1 < W < 3.1$ GeV. The fit is constrained by the high precision longitudinal and transverse separated cross section measurements from Jefferson Lab Hall C, un-separated Hall C measurements up to $Q^2$ 7.5 GeV$^2$, and photoproduction data at $Q^2 = 0$. Compared to previous fits, this fit covers a wider kinematic range, fits both transverse and longitudinal cross sections, and features smooth transitions to the photoproduction data at $Q^2 = 0$ and DIS data at high $Q^2$ and W.

The electron rates on nuclear targets were calculated using the cross section model of P.E. Bosted and V. Mamyan [24]. This is an empirical fit to electron-nucleus scattering for $A > 2$ based on world data. It is valid for $0 < W < 3.2$ GeV and $0.2 < Q^2 < 5$ GeV$^2$. The fit is based on previous empirical fits to electron-proton and electron-neutron scattering, but takes into account the effects of Fermi motion, meson exchange currents and Coulomb corrections. A comparison of this model to JLab inclusive electron-nucleus cross section data on iron, aluminum, hydrogen, deuterium, beryllium, carbon and gold [8, 25] is shown in Figure 12 in a $Q^2$ range that matches the coverage of our proposed measurements. There is good agreement between model and measurements for both data sets. We also estimated the rates of pion production in the target using the model of P.E. Bosted [26] based on the fit by Wiser to charged pion production from SLAC [27].

In Table IV we show limits on the electron and pion rates calculated with the models described above for a given beam current for individual $x$ settings. For each fixed central $x$ there are one or several central $Q^2$ settings each of those, in turn, corresponding to four or more central beam energy, spectrometer momentum and angle settings ($E_B$,$E_p$,$\theta$) as shown in Tables I, II and III. Thus for a given central $x$ we calculated the electron and pion rates for individual ($Q^2$,$E_B$,$E_p$,$\theta$) settings taking into account the spetcrometers acceptance (i.e. rates have been integrated over the spetcrometers acceptance as indicated in Figure 11) and in Table IV we show an upper rate limit for a given beam current. Our goal was to keep the raw detector rates below 600 kHz so we used the beam current setting as leverage to control the rate. At high rates the running time will be driven by the data acquisition system rate limit

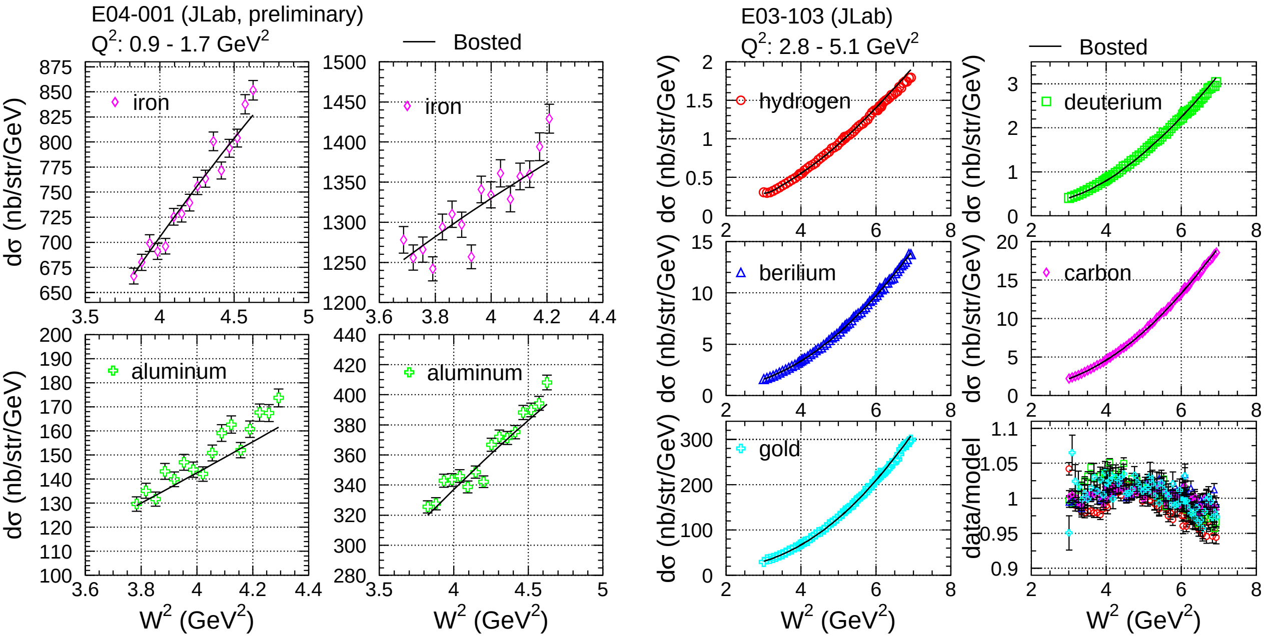

FIG. 12: **Left:** Comparison of P.E. Bosted and V. Mamyan [24] cross section model used for nuclear targets rate calculations to Hall C measurements on Iron and aluminum from experiment E04-001 [8]. **Right:** Comparison of the same model to inclusive electron-nucleus cross sections on deuterium, beryllium, carbon, and gold from Hall C experiment E03-103 [25]. Comparisons to data from a hydrogen target are also shown.

| $x$ | $I_B(H)$ | $R(H)$ | $I_B(D)$ | $R(D)$ | $I_B(Be)$ | $R(Be)$ | $I_B(C)$ | $R(C)$ | $I_B(Cu)$ | $R(Cu)$ | $I_B(Ag)$ | $R(Ag)$ | $I_B(Au)$ | $R(Au)$ |
|---|---|---|---|---|---|---|---|---|---|---|---|---|---|---|
| 0.100 | 60 | <216 | 40 | <206 | 20 | <157 | 30 | <150 | 60 | <85 | 60 | <66 | 60 | <50 |
| 0.125 | 60 | <259 | 40 | <339 | 20 | <317 | 30 | <311 | 60 | <187 | 60 | <144 | 60 | <109 |
| 0.150 | 60 | <388 | 40 | <519 | 20 | <513 | 30 | <506 | 60 | <307 | 60 | <237 | 60 | <180 |
| 0.175 | 60 | <538 | 30 | <535 | 15 | <535 | 25 | <589 | 60 | <427 | 60 | <329 | 60 | <250 |
| 0.200 | 50 | <555 | 25 | <554 | 13 | <582 | 20 | <590 | 60 | <529 | 60 | <406 | 60 | <306 |
| 0.225 | 60 | <294 | 50 | <476 | 30 | <568 | 45 | <563 | 60 | <224 | 60 | <172 | 60 | <129 |
| 0.250 | 60 | <178 | 60 | <341 | 40 | <449 | 60 | <446 | 60 | <132 | 60 | <101 | 60 | <76 |
| 0.275 | 60 | <195 | 60 | <376 | 40 | <496 | 60 | <492 | 60 | <145 | 60 | <111 | 60 | <83 |
| 0.300 | 60 | <199 | 60 | <383 | 45 | <571 | 60 | <503 | 60 | <149 | 60 | <113 | 60 | <85 |
| 0.400 | 60 | <75 | 60 | <140 | 60 | <275 | 60 | <182 | 60 | <53 |  |  | 60 | <30 |
| 0.500 | 60 | <12 | 60 | <22 | 60 | <41 | 60 | <27 | 60 | <8 |  |  |  |  |
| 0.600 |  |  | 60 | <3 | 60 | <5 | 60 | <4 | 60 | <1 |  |  |  |  |

TABLE IV: Beam current, $I_B$, in $\mu$A and total particle rates, $R$, in kHz for all targets. The rate limits shown include both electron and pion rates. The beam current has been chosen for each kinematic point to keep the detector rates below 600 kHz to ensure good reconstruction of tracks in a high-rate environment.

(3 kHz at most with the 12 GeV Hall C equipment) however it is important to use a beam current setting that limits raw detector rates to values that could be handled without an added ambiguity in the tracking reconstruction and identification in high-rate environments.

### C. Backgrounds and Corrections to the Measured Cross Sections

In what follows we will discuss our estimates of contributions from radiative corrections, Coulomb corrections and charge symmetric backgrounds to the cross sections at the proposed kinematics. We will also show our predictions for the pion-to-electron ratios. The magnitude of backgrounds and corrections like the radiated quasielstic contribution to the proposed measurements or the charge symmetric background will be taken into account when estimating the running time to achieve a certain statistical precision. Multiplicative corrections like Coulomb corrections or the inelastic radiative contributions will not affect the **relative** statistical precision but the accuracy in their estimation will affect the overall systematic uncertainty. Where possible we propose additional measurements to ensure a precise knowledge of these corrections.

### 1. *Radiative Corrections*

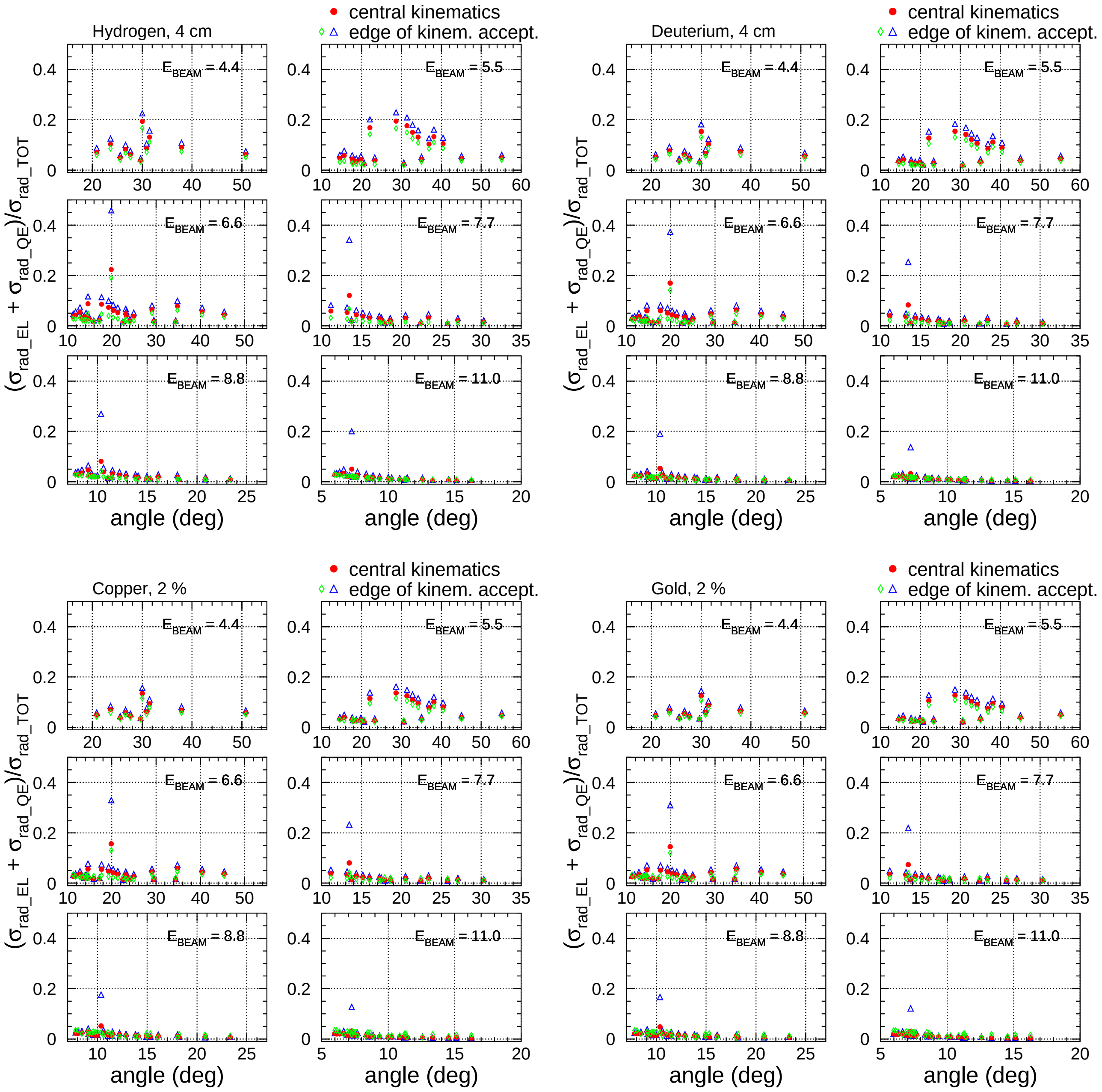

FIG. 13: Estimates of the radiated elastic and quasielastic contributions to the total cross section using the formalism of Mo and Tsai [28] that accounts for external and internal radiative effects. The estimates are shown at the central kinematics (red full circles) but also at the kinematics corresponding to the spectrometers acceptance edges (empty green circles and blue triangles). The radiative effects are shown for the cryogenic 4 cm hydrogen and deuterium targets as well as for the 2% r.l. solid targets copper and gold.

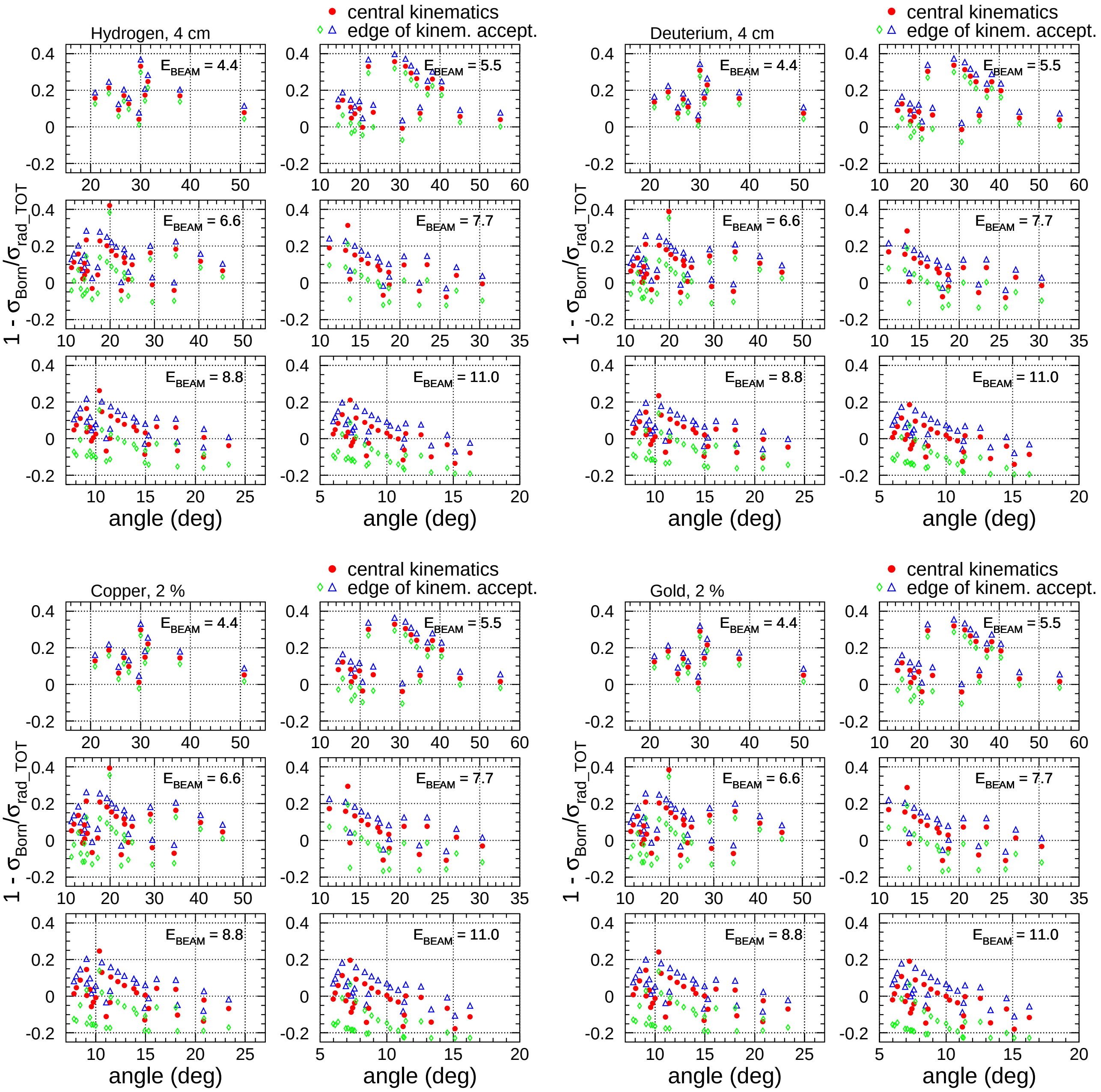

FIG. 14: Estimates of the total radiative effects using the formalism of Mo and Tsai [28] for external and internal radiative effects. The estimates are shown at the central kinematics (red full circles) but also at the kinematics corresponding to the spectrometers acceptance edges (empty green circles and blue triangles). The radiative effects are shown for the cryogenic 4 cm hydrogen and deuterium cryogenic targets as well as for the 2% r.l. solid targets copper and gold.

In order to determine the differential cross section that accounts just for the one photon exchange process (the Born cross section), all other contributions from higher order processes in the electromagnetic running coupling constant have to be calculated and corrected for in the measured cross section. Higher order processes include vacuum polarization (the exchanged photon creates particle-antiparticle pairs), vertex processes (a virtual photon is emitted and reabsorbed), Bremsstrahlung emission of real photons, multi-photon exchange. The radiative processes can be divided into two main categories: internal and external. The internal effects take place at the scattering vertex and include internal Bremsstrahlung, vacuum polarization, vertex processes and multiple photon exchange. The external processes (Bremsstrahlung) occur within the target material before or after the primary scattering takes place and are dependent on the target thickness. All the processes described above will lead to energy changes of the incoming and/or the scattered electron.

To obtain the Born inelastic cross section, the radiated elastic/nuclear elastic and quasielastic cross sections are typically subtracted while the inelastic radiative effects are corrected multiplicatively as follows:

$$\sigma^{nuclear}_{Born} = (\sigma_{measured} - \sigma^{model}_{elastic\,radiated} - \sigma^{model}_{quasielastic\,radiated}) * \frac{\sigma^{model}_{inelastic\,Born}}{\sigma^{model}_{inelastic\,radiated}}. \tag{11}$$

For our proposed kinematics the radiated elastic and quasielastic contributions to the total cross section have been calculated using a code based on the formalism by Mo and Tsai [28] that calculates both the internal and external radiative effects. In Figure 13 we show our estimates for 4cm hydrogen and deuterium cryogenic targets and for the 2% r.l. copper and gold solid targets at the central kinematics (red full circles) but also at the kinematics that correspond to the edges of the spectrometers acceptance (green empty circles and blue triangles). For a given scan ($E_B$,$E_p$,$\theta$) one acceptance limit is set by the momentum bite of the spectrometer while the other limit by the $W^2$ cut of 3 GeV$^2$ (as indicated by the dashed line in Figure 11) since our physics goals focus on the DIS region. We can see that for the kinematic settings at beam energies of 7.7, 8.8 and 11 GeV the correction is well within 10% for all targets while for the lower beam energies within 20%. Thus a 1% uncertainty in the elastic and quasielastic cross section would lead to at most 0.2% uncertainty in the Born inelastic cross section.

The inelastic radiative effects are not sensitive to the $\epsilon$ change and therefore do not affect the extraction of $R$ but to set a scale we calculated the total radiative effects at our proposed kinematics and we show our results in Figure 14. In all cases the total radiative corrections will be no large than 40%. To test our understanding of the external radiative effects we propose to take measurements for few kinematic points with a 6% r.l. copper target. The magnitude of the external radiative corrections would scale with the radiation length of the target but after accounting for radiative effects the difference in the extracted cross sections, if any, would be a measure of the systematic uncertainty of this correction. We would thus perform the same measurements on a 6% r.l. copper target as with the production 2% r.l. one at $x$ of 0.1, 0.275 and 0.4. Details of these measurements are given in Table V.

| $x$ | $I_B$ ($\mu A$) | $R$ (KHz) | $\delta$(%) | time (hours) | $\pi/e$ |
|---|---|---|---|---|---|
| 0.100 | 60 | <258 | 0.45 | 0.6 | <4 |
| 0.275 | 60 | <437 | 0.45 | 2.6 | <4 |
| 0.400 | 60 | <159 | 0.45 | 4.5 | <3 |

TABLE V: Beam current, $I_B$, in $\mu$A, detector rates, $R$, in kHz, projected statistical uncertainty, $\delta$, in % and time estimates for a 6% copper target. The rate limits shown include both electron and pion rates. The time is calculated with the limit of 3 kHz coming from the data acquisition system. The data would be used to verify the accuracy of the external radiative corrections.

### 2. *Charge-Symmetric Background*

There is a potentially significant probability for neutral pion production in the targets as a result of the interaction with the electron beam. These neutral pions can decay into high energy photons. Another source of photons could be the Bethe-Heitler process. The photons thus produced can further convert into $e^+e^-$ pairs in the target materials or in the materials preceding the detectors contributing to the primary scattered electron yield. This background being charge-symmetric can be measured directly by changing the polarity of the spectrometers to positive and measuring the produced positrons.

We estimated the possible contribution of the background comming from neutral pion production in the target at all our proposed kinematics and the results are shown in Figure 15 for deuterium and gold. We used the model of P.E. Bosted [26] which employs the fit to the charged pion production data accumulated at SLAC [27]. The neutral pion production is estimated as an average of the positive and negative pion production. The positron cross section is calculated using the decay branching ratios for a neutral pion and the radiation length of the material where a photon that results from the decay can produce $e^+e^-$ pairs. It was found that this model describes fairly well the momentum dependence of the positron cross section for some of the 6 GeV runs [29].

We found that the background contribution to the primary scattered electron yield is no larger than 20%. We plan to measure the charge symmetric background at beam energies of 4.4, 5.5, and 6.6 GeV with few measurements for checks at 7.7, 8.8 and 11 GeV. To estimate the total running time we assume 10% of the production time on each target.

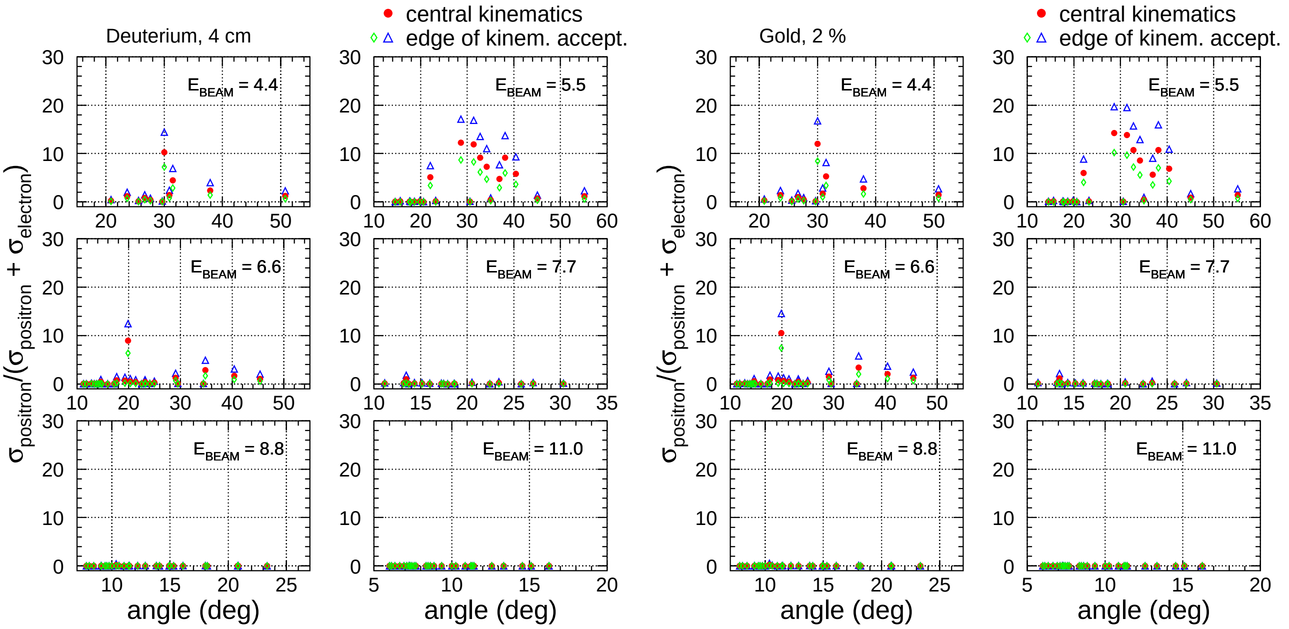

FIG. 15: Charge-symmetric background estimates for deuterium and gold targets for all the proposed kinematics. The calculations are shown at the central kinematics (red full circles) but also at the kinematics corresponding to the spectrometers acceptance edges (empty green circles and blue triangles).For a given scan ($E_B$,$E_p$,$\theta$) one acceptance limit is set by the momentum bite of the spectrometer while the other limit by the $W^2$ cut of 3 GeV$^2$ (as indicated by the dashed line in Figure 11) since our physics goals focus on the DIS region.

### *3. Coulomb Corrections*

Though the Coulomb corrections can be neglected in DIS at very high incident beam energies, for energies in the range of the earlier data from SLAC or at JLab, the Coulomb distortion could result in a non-negligible correction to the cross section. This process refers to the acceleration (deceleration) of the incident (scattered) electrons in the Coulomb field created by nearby protons inside a nucleus via the exchange of soft photons. The net result is a change in the incident and scattered electron kinematics but also a focusing of the electron wave function in the interaction region. Thus the cross sections calculation within the Plane Wave Born Approximation (PWBA) formalism is no longer sufficient and a treatment within the Distorted Wave Born Approximation (DWBA) would be more suitable. However, full DWBA calculations are difficult to implement so typically a more convenient formalism is used: the Effective Momentum Approximation (EMA). In this approximation the incident ($E$) and scattered ($E_p$) electron energies are shifted by an average Coulomb potential $\delta E$ while the focusing factor, $(E + \delta E)/E$ enters quadratically in the cross section calculation. A detailed comparison of the EMA approach and the full DWBA calculation in the quasi-elastic region was performed by Aste and collaborators [30] and it was concluded that the two methodes agree fairly well. However, the EMA approach has never been tested in the DIS region [7].

We calculated the Coulomb corrections within the EMA framework for our proposed central kinematics and the magnitude of the correction is shown in Figure 16 for carbon and gold targets. We see that for a low Z target as carbon the correction is rather small but for a large Z target as gold it could reach up to 9% at some of our kinematics. We thus propose to test the EMA approach in the DIS region by measuring ratios of gold to deuterium cross sections at fixed $x$ and $\epsilon$ but varying $Q^2$ as shown in Table VI. The kinematics have been chosen such that for a fixed $x$ and $\epsilon$ the Coulomb corrections will vary significantly between the two $Q^2$ settings. The expectation is that a measured change in the cross section ratio could only be due to the change in Coulomb distortion effects since the nuclear targets to deuterium cross section ratios have been shown to approximately scale with $Q^2$ [25]. Such test would require a very good understanding of other corrections and backgrounds. Our calculations of the radiative corrections, the $pi/e$ ratio and the charge-symmetric background are shown in Table VII. We would measure the charge symmetric background at the low $\epsilon$ setting. We would also take short runs on an aluminum (dummy) target to measure the background comming from the deuterium cryogenic target walls.

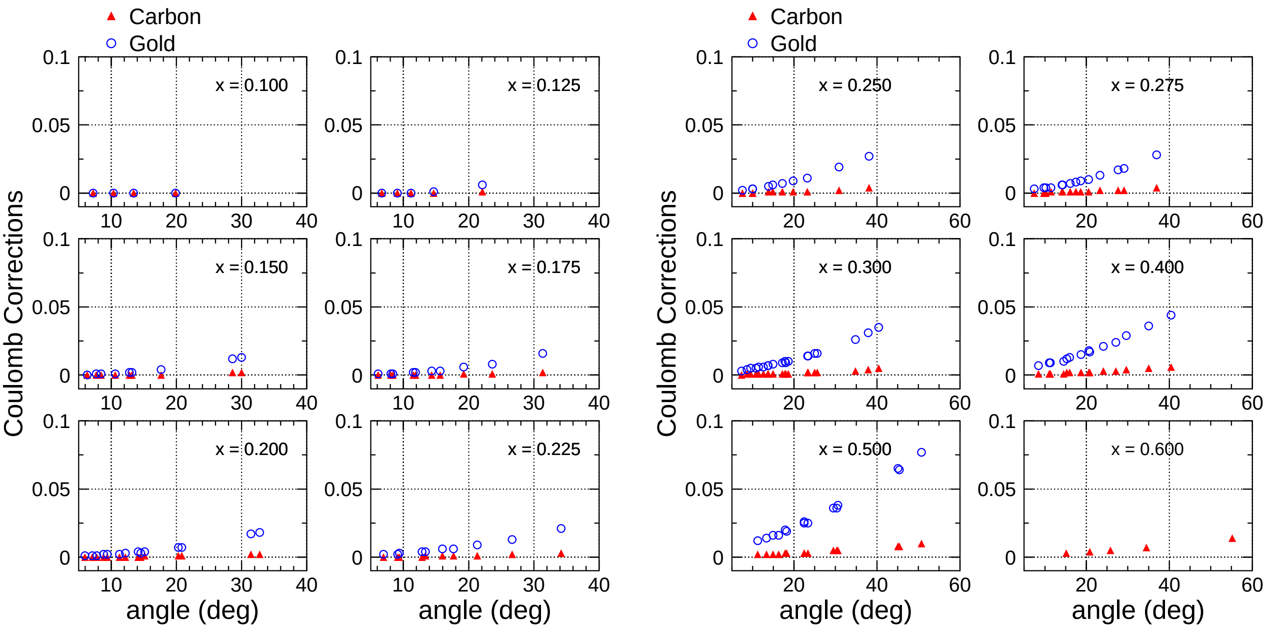

FIG. 16: Coulomb corrections estimated within the EMA framework for carbon and gold targets.

| $Q^2$ | $x_b$ | $E$ | $E'$ | $\theta$ | $\epsilon$ | y | W | $C^{Au}_{\text{Coulomb}}$ | R$^D$ (Hz) | Time$^D$ (h) | R$^{Au}$ (Hz) | Time$^{Au}$ (h) |
|---|---|---|---|---|---|---|---|---|---|---|---|---|
| 3.48 | 0.50 | 4.4 | 0.69 | 64.6 | 0.20 | 0.84 | 2.08 | 11.6% | 23.9 | 1.2 | 4.1 | 3.4 |
| 9.03 | 0.50 | 11.0 | 1.38 | 45.5 | 0.20 | 0.88 | 3.10 | 6.2% | 10.5 | 2.7 | 1.8 | 7.8 |
| 2.15 | 0.50 | 4.4 | 2.11 | 27.9 | 0.70 | 0.52 | 1.74 | 3.5% | 1.31k | 0.3 | 223 | 0.3 |
| 5.79 | 0.50 | 11.0 | 4.83 | 19.0 | 0.70 | 0.56 | 2.58 | 1.9% | 662 | 0.3 | 114 | 0.3 |

TABLE VI: The event rates, beam time as well as the Coulomb correction for the Coulomb scan test data. Rates assume 60 $\mu$A on a 4 cm deuterium cell and a 2% radiation length gold target. Times are for 100k (50k) events for deuterium (gold) at the $\epsilon = 0.2$ settings. We will take short run (0.3 h) with dummy target for deuterium background subtraction.

| $\epsilon$ | $Q^2$ | Target | $RAD.CORR.$ | $\pi/e$ | Charge-symmetric Background |
|---|---|---|---|---|---|
| 0.2 | 3.48 | D | 1.17 | 161 | 0.108 |
| 0.2 | 9.03 | D | 1.11 | 106 | 0.043 |
| 0.2 | 3.48 | Au | 1.11 | 6.1 | 0.180 |
| 0.2 | 9.03 | Au | 1.09 | 1.8 | 0.076 |
| 0.7 | 2.15 | D | 0.96 | 6.2 | 0.0 |
| 0.7 | 5.79 | D | 0.94 | 0.6 | 0.0 |
| 0.7 | 2.15 | Au | 0.93 | 1.4 | 0.0 |
| 0.7 | 5.79 | Au | 0.91 | 0.2 | 0.0 |

TABLE VII: Backgrounds and radiative corrections factors for Coulomb correction scan settings. Dominant backgrounds are from pion contamination and charge symmetric processes. A 2% gold target has been chosen to minimize (external) radiative corrections and contributions from the charge symmetric backgrounds.

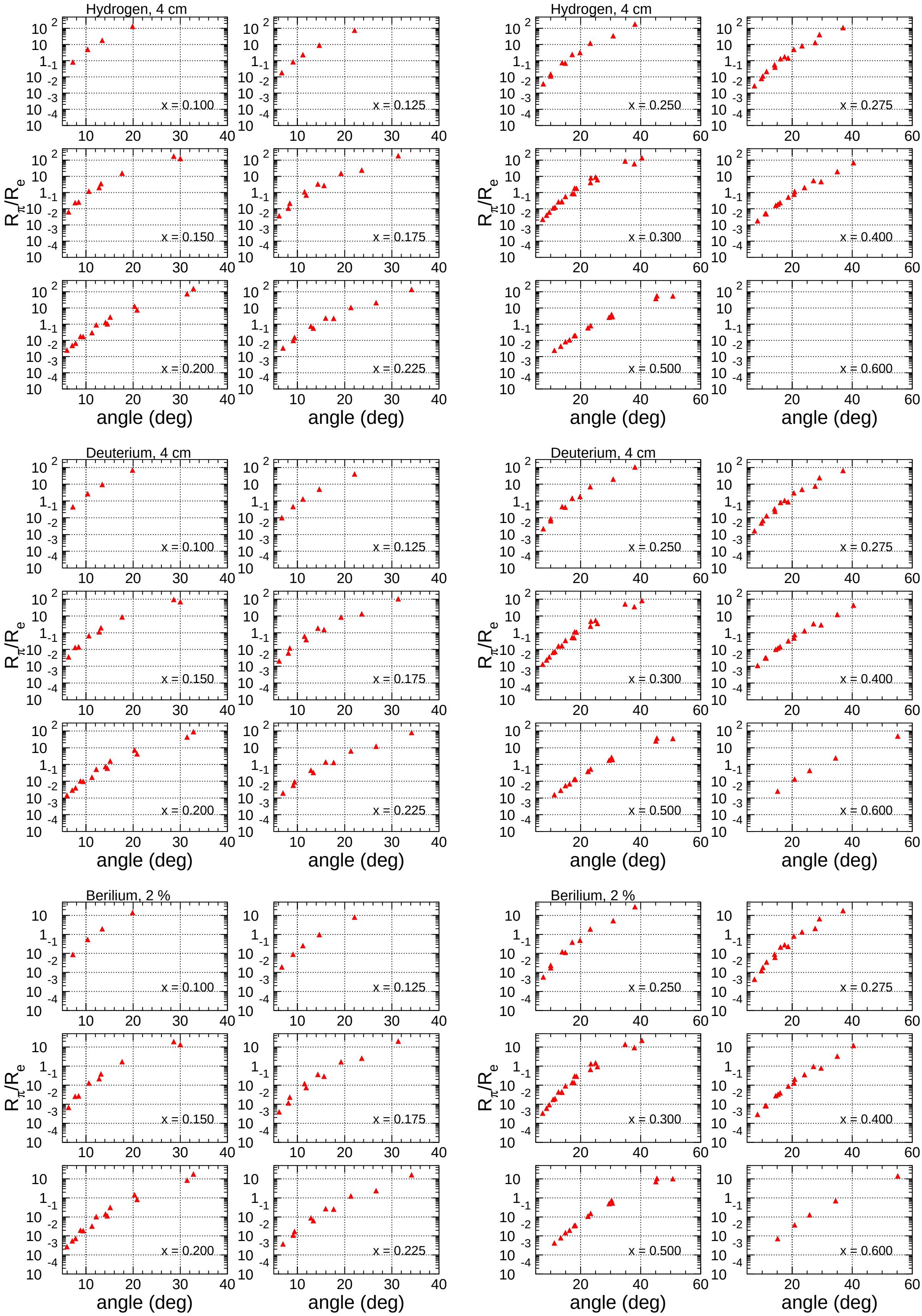

FIG. 17: Pion-to-electron ratios for hydrogen, deuterium and beryllium.

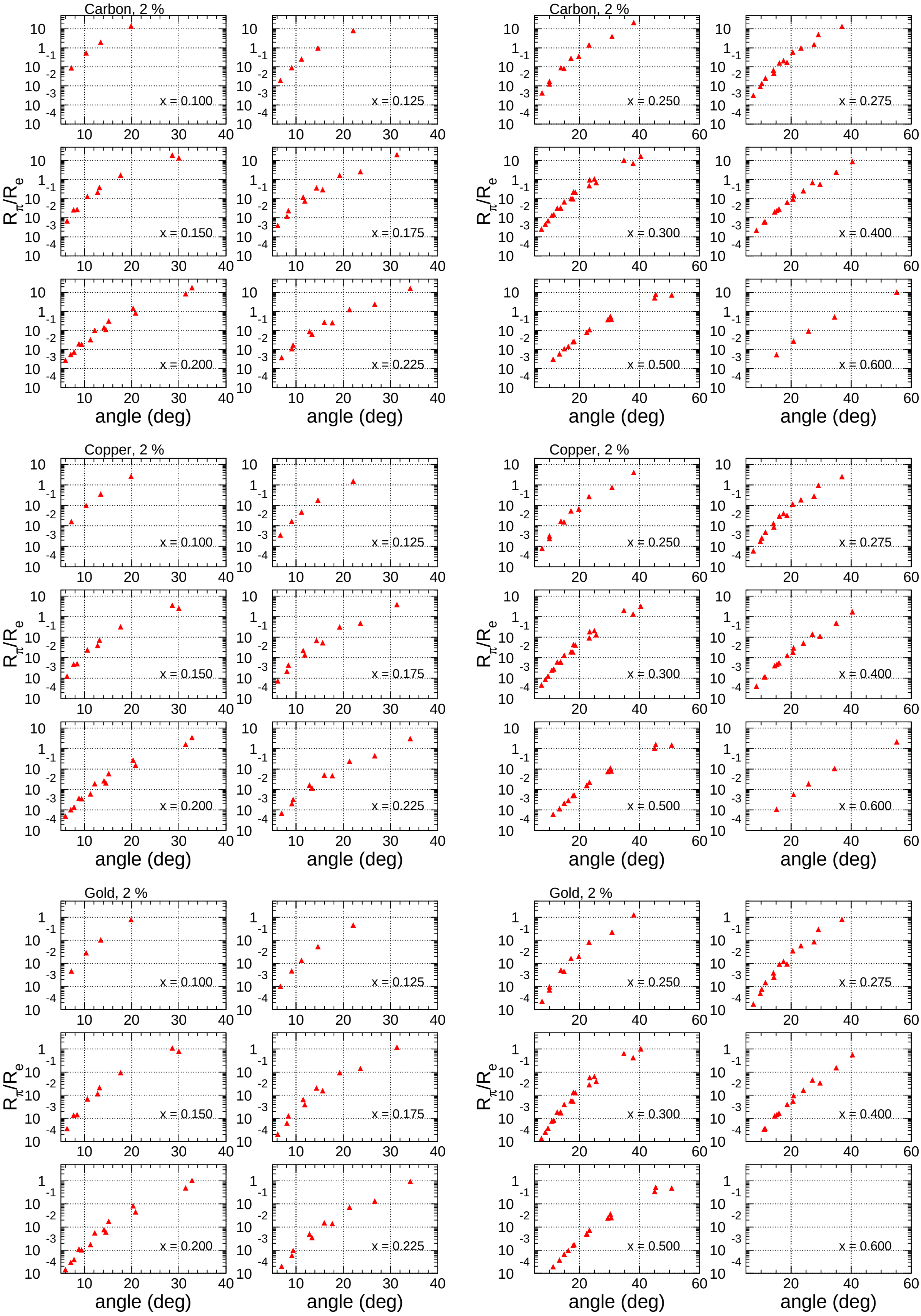

FIG. 18: Pion-to-electron ratios for carbon, copper and gold.

### *4. Estimates of Pion-to-Electron Ratio*

The $\pi/e$ ratios have been estimated for all the central kinematics with the model of P.E. Bosted [26] based on Wiser's fit [27] and it is shown in Figures 17 and 18. For hydrogen the highest ratio is about 200. With a pion rejection factor of $10^{-4}$ , the contribution of the $\pi^-$ background to the cross section would be less than 2%. For the deuterium target the highest ratio is 100 which would lead to at most 1% pion background. For all the other nuclear targets the pion contamination would be at the subpercent level. The subtraction of the charge symmetric background will further reduce the pion background.

## D. Beam-time Request

In Table VIII we show the statistical precision goal ($\delta$ in %) and the required production running time for hydrogen, deuterium, beryllium, carbon, copper, silver and gold targets. Due to rate limitations, for gold we will only measure the $Q^2$ settings of 2 and 3 GeV$^2$ at $x = 0.4$. As explained in the Subsection **Kinematics** and as shown in Figure 11, for a given central kinematic setting defined by $(x, Q^2, E_B, E_p, \theta)$ we bin the momentum acceptance of the spetcrometers in bins corresponding to a size in $W^2$ of 0.1 GeV$^2$ (in Figure 11 each such bin is shown as an empty circle). The statistical precision shown in Table VIII is targeted for each such individual bin in the kinematic region of $W^2 > 3$ GeV$^2$. This will allow us to extract the physics quantities with unprecedented statistical precision not only at the central kinematics (indicated by black stars in Figure 11) but also anywhere in the spectrometers acceptance where there is an overlap of at least two or three beam energy settings. Such extractions would require only small $Q^2$ corrections. The production running times were estimated by assuming an excess of 25% more events than required by our statistical goal in order to account for backgrounds that would be subtracted from the measured cross section and thus would modify the statistical uncertainty (like, for example, the radiated quasielastic controbution, the charge symmetric background or the contribution from the cryogenic target walls).

| $x$ | $\delta(H)$ | $t(H)$ | $\delta(D)$ | $t(D)$ | $\delta(Be)$ | $t(Be)$ | $\delta(C)$ | $t(C)$ | $\delta(Cu)$ | $t(Cu)$ | $\delta(Ag)$ | $t(Ag)$ | $\delta(Au)$ | $t(Au)$ |
|---|---|---|---|---|---|---|---|---|---|---|---|---|---|---|
| 0.100 | 0.5 | 0.6 | 0.2 | 2.9 | 0.3 | 1.2 | 0.35 | 0.97 | 0.45 | 0.6 | 0.45 | 0.6 | 0.45 | 0.7 |
| 0.125 | 0.5 | 0.7 | 0.2 | 3.8 | 0.3 | 1.6 | 0.35 | 1.3 | 0.45 | 0.8 | 0.45 | 0.8 | 0.45 | 0.9 |
| 0.150 | 0.5 | 1.4 | 0.2 | 7.4 | 0.3 | 3.2 | 0.35 | 2.7 | 0.45 | 1.7 | 0.45 | 1.8 | 0.45 | 2 |
| 0.175 | 0.5 | 1.5 | 0.2 | 8.5 | 0.3 | 3.7 | 0.35 | 3 | 0.45 | 1.9 | 0.45 | 2 | 0.45 | 2.3 |
| 0.200 | 0.5 | 2.3 | 0.2 | 12.8 | 0.3 | 5.6 | 0.35 | 4.6 | 0.45 | 2.8 | 0.45 | 3 | 0.45 | 3.4 |
| 0.225 | 0.5 | 1.7 | 0.2 | 8.6 | 0.3 | 3.7 | 0.35 | 3 | 0.45 | 2.2 | 0.45 | 2.5 | 0.45 | 3 |
| 0.250 | 0.5 | 2 | 0.2 | 9.1 | 0.3 | 3.9 | 0.35 | 3.2 | 0.45 | 2.8 | 0.45 | 3.3 | 0.45 | 4.1 |
| 0.275 | 0.5 | 2.8 | 0.2 | 12.7 | 0.3 | 5.3 | 0.35 | 4.4 | 0.45 | 4 | 0.45 | 4.8 | 0.45 | 6 |
| 0.300 | 0.5 | 4.8 | 0.2 | 20.4 | 0.3 | 8 | 0.35 | 6.8 | 0.45 | 7.2 | 0.45 | 9 | 0.5 | 9.6 |
| 0.400 | 0.5 | 6 | 0.25 | 16.1 | 0.3 | 6.8 | 0.35 | 6.9 | 0.45 | 10.7 | | | 0.5 | 5 |
| 0.500 | 0.5 | 19 | 0.3 | 28 | 0.3 | 16 | 0.35 | 18.8 | 0.5 | 31.3 | | | | |
| 0.600 | | | 0.3 | 27.7 | 0.3 | 15 | 0.35 | 18.7 | 0.5 | 32.9 | | | | |
| total | | 43 | | 158 | | 74 | | 74 | | 99 | | 28 | | 37 |

TABLE VIII: Statistical precision goals ($\delta$ in %) and the required production running times ($t$ in hours) for hydrogen, deuterium, beryllium, carbon, copper, silver and gold. The running times are summed up at a fixed $x$ over all $Q^2$ settings. The total production running time is also shown for each target individualy summing over all kinematics. The time estimates shown do not include the aluminum dummy running time.

In Table IX we present our beamtime request. We would need a total of 513 hours for production running on all targets to achieve the statistical precision specified in Table VIII. The external radiative corrections checks and the Coulomb correction scans would require in addition 9 and 20 hours, respectively (please see previous subsections). To measure the background contribution to the hydrogen and deuterium yield coming from the cryogenic target walls we need 15 hours (10% of the total production running time on deuterium). To measure the charge symmetric background we assumed a 10% running time of the production time and this would amount to roughly 50 hours. We estimate that we would need 66 hours for various calibrations of the spectrometers and other equipement. We also plan to measure few scans with both spectrometers where possible for cross-calibration. This type of experiment requires many configuration changes. For each beam energy change the beam optics would have to be verified so we assume 0.4 hours for each beam energy change which leads to a total of 24 hours. We counted 130 momentum and

| Category | Activity | Beam Time (Hours) |
|---|---|---|
| Production | $R$ Measurements on H, D, Be, C, Cu, Ag, Au | 513 |
| Calibrations and Backgrounds | Radiative Corrections Checks | 9 |
| | Coulomb Corrections Checks | 20 |
| | Cryogenic Traget Walls Background Measurements | 15 |
| | Optics (Sieve/Open Collimator; $P/\theta$ scan ) | 24 |
| | Elastic Scattering on H | 12 |
| | Beam Energy Measurements (6) | 12 |
| | Beam Current Calibration | 8 |
| | Horizontal Beam Position Scan on H/D | 2 |
| | Target Boiling/Rates Studies | 8 |
| | SHMS and HMS cross-calibration | 6 |
| | Charge Symmetric Background Measurements | 50 |
| Others | Beam Pass Changes | 24 |
| | Target Changes | 98 |
| | Momentum and Angle Changes | 43 |
| Total | | 844 (35 days) |

TABLE IX: Beam time request assuming 100% efficiency.

angle changes. We assume that the momentum and the angle of the spectrometers could be changed simultaneously so with an allocated time of 20 minutes per change this would amount to 43 hours. Finally, we will have roughly 980 target changes and assuming 6 minutes per change we would need an additional 98 hours. In total we need 844 hours or 35 days assuming 100% running efficiency.

### E. Impact of Proposed Measurements

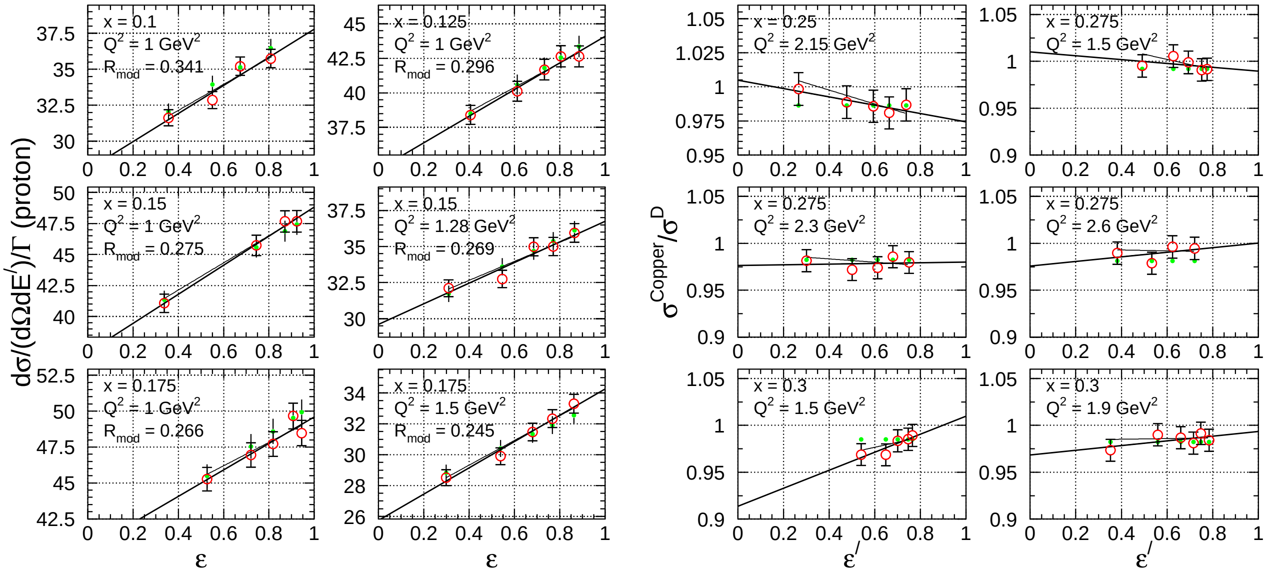

FIG. 19: **Left:** An example of LT separations at fixed ($x$, $Q^2$) on a proton target. The $\epsilon$ dependence of the radomized reduced cross section $d\sigma/\Gamma$ is fitted and $\sigma_L$, $\sigma_T$ and $R_p$ and their fit uncertainties are extracted. **Right:** An example of projected uncertainties extraction for $R_{Cu} - R_D$.

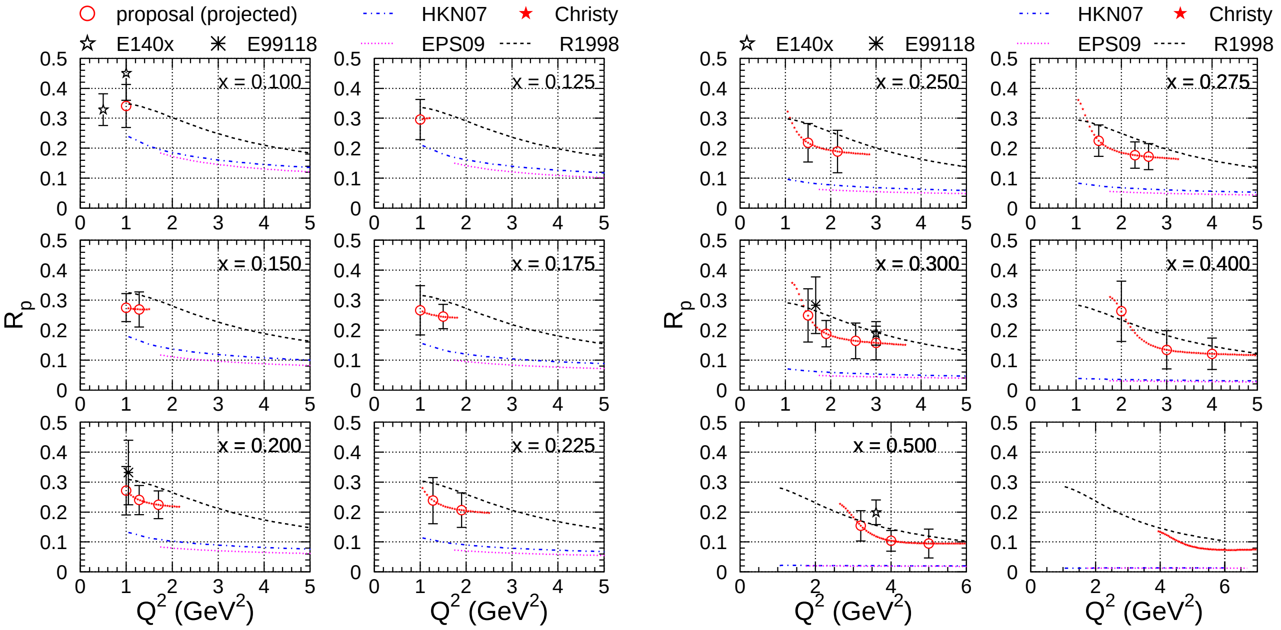

FIG. 20: Projected systematic uncertainties (empty red circles) in the $R_p$ extraction at all the proposed central kinematics. Parametrizations of $R_p$ from R1998 [33] (black curve), M.E. Christy model [23] (red curve), HKN07 [17] (blue curve) and EPS09 [18] pink curve are also shown. Existing true Rosenbluth LT separations in DIS from SLAC and JLab are displayed in black symbols. For our simulated extractions the model of M.E. Christy has been used as input.

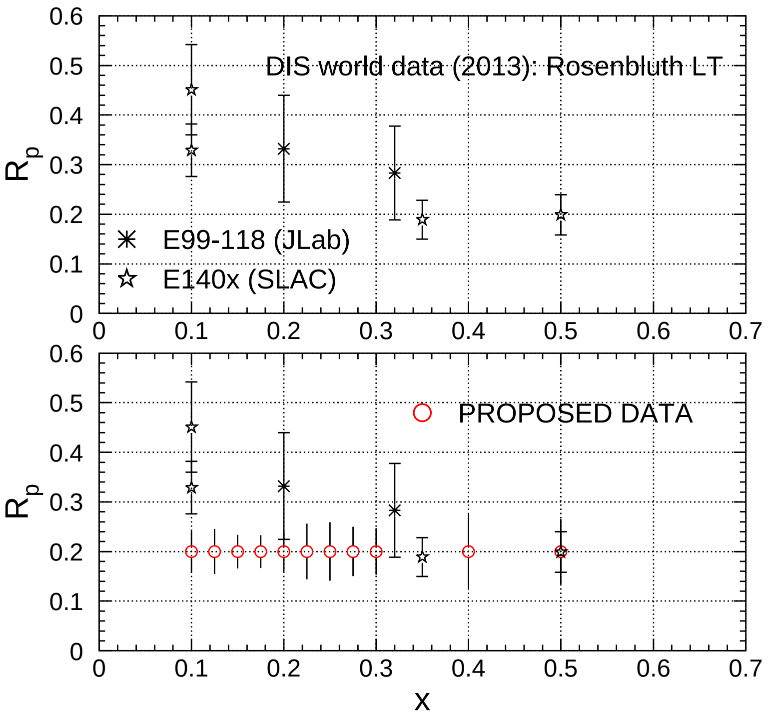

FIG. 21: Projected systematic uncertainties on the $R_p$ extraction as a function of $x$ at all proposed central kinematics. Similar extractions of $R$ will be performed on deuterium, beryllium, carbon, copper, silver and gold.

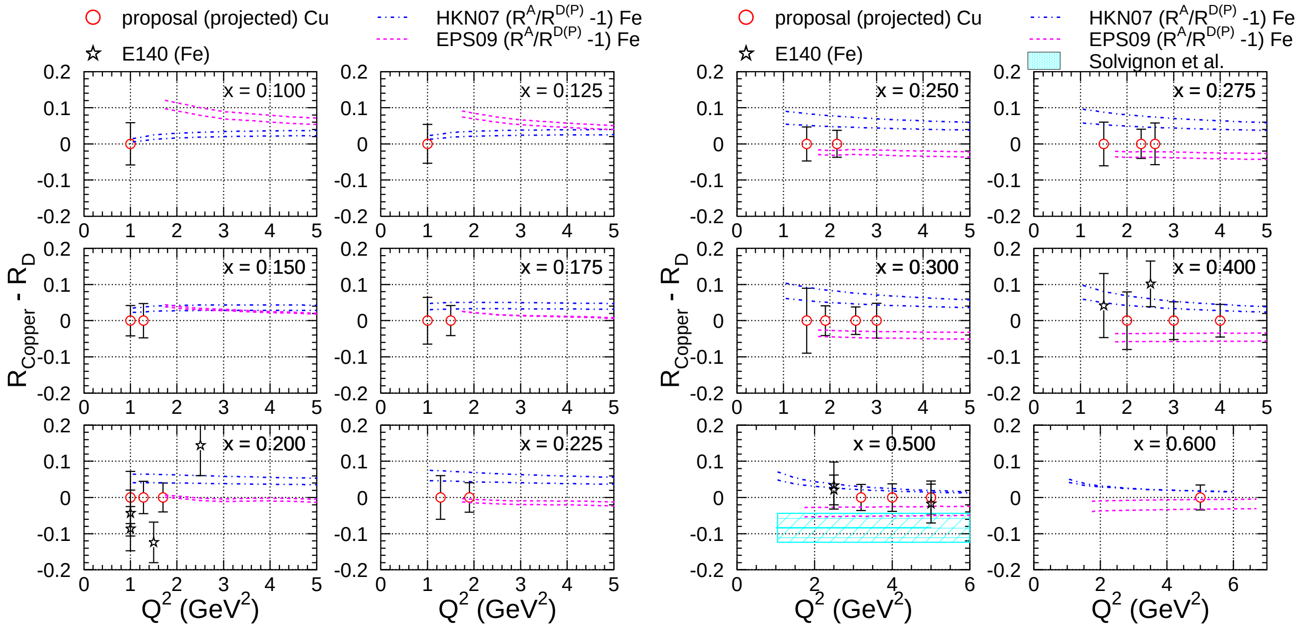

FIG. 22: Projected systematic uncertainties (empty red circles) in the $R_{Cu} - R_D$ extraction at all the proposed central kinematics. Parametrizations for an Iron target from HKN07 [17] (blue curve) and EPS09 [18] pink curve are also shown. Existing true Rosenbluth LT separations in DIS from SLAC E140 are displayed in black symbols. Additionally an extraction of $R_{Fe} - R_D$ and its uncertainty by Solvignon and collaborators [7] from re-analyzed SLAC E140 data to include Coulomb corrections is represented by the cyan band. For our simulated separations the model of P.E. Bosted and V. Mamyan [24] has been used as input.

In what follows we discuss the impact of our proposed data and we will use as example the extraction of $R_p$ from the hydrogen target proposed measurements and that of $R_{Cu} - R_D$ from the deuterium and copper projected data. We used the model of M.E. Christy [23] and that of P.E. Bosted and V. Mamyan [24] to calculate the proton reduced cross sections and the ratios $\sigma_A/\sigma_D$, respectively. We assume that we are dominated by systematics and that we can achieve the same systematic accuracy in our extraction of cross sections as the 6 GeV Rosenbluth LT experiments [31, 32] (a table with the systematics of the 6 GeV experiments can be found in the Appendix). Thus for the extraction of $R_p$ we use a systematic uncertainty of 1.8% on the cross section while for the cross section ratio which enters in the calculation of $R_{Cu} - R_D$ we assume 1.1%.

In Figure 19 we show examples of Rosenbluth LT separations on hydrogen (left panel) and of $R_{Cu} - R_D$ extractions from fits of cross section ratios according to Equation 8. To extract $R_p = \sigma_L/\sigma_T$ first we produce the reduced cross sections from M.E. Christy model at each $\epsilon$ point for a given fixed ($x$, $Q^2$) kinematic setting. The reduced cross sections, $d\sigma/\Gamma$, thus produced are represented by the green full circles in Figure 19, left panel, and it can be seen that they follow a straight line in the $(d\sigma/\Gamma, \epsilon)$ phase space for a fixed ($x$, $Q^2$) as expected from a Rosenbluth extraction. The next step is to estimate the projected precision of our extractions so we randomize the reduced cross section (according to a gaussian distribution) assuming a 1.8% ($\epsilon$) point-to-point systematic uncertainty (the precision achieved by the 6 GeV Rosenbluth LT experiments) and the resulting cross sections are shown as red empty circles in Figure 19. We then perform a fit of the randomized reduced cross sections with $\epsilon$ and extract $\sigma_L$, $\sigma_T$, $R$ and their projected uncertainties as the fit uncertainties. To estimate the unceratinty coming from using two different spectrometers complementarly for one LT extraction, we redo the fit varying the HMS reduced randomized cross sections by 1% (we assume that we will cross-calibrate the SHMS and HMS to the 1% precision level). The difference in results between the two fits is then included in the total uncertainty.

A similar procedure was followed to propagate the projected systematic poin-to-point uncertainty of 1.1% on the nuclear targets to deuterium ratios into the extraction of $R_A - R_D$. We use the model of P.E. Bosted and V. Mamyan [24] to calculate $\sigma_A/\sigma_D$ at our kinematics. This ratio without randomization is represented in Figure 19, right panel, by the full green circles. By construction, at a fixed $x$ and $Q^2$ the ratio has no $\epsilon^{'}$ dependence. After the randomization (empty red circles) an artificial slope may result but this is not the relevant quantity. We fit the randomized ratio with a fit function given by Equation 8 with $\sigma_T^A/\sigma_T^D$ and $R_A - R_D$ as fit parameters. The relevant quantity we extract is the fit uncertainty on $R_A - R_D$ which connects the projected point-to-point uncertainties on the cross section ratios that we would measure to the physics quantity we would extract.

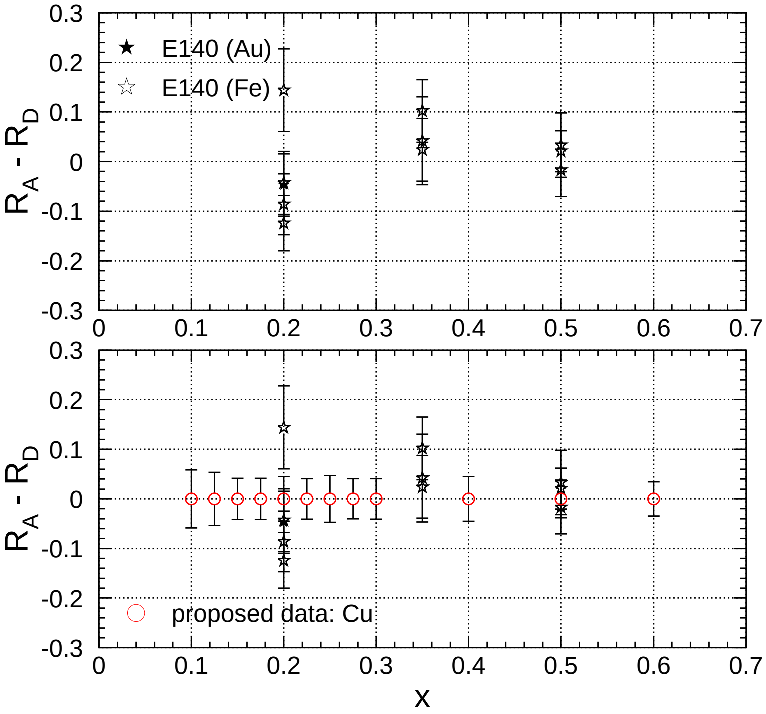

FIG. 23: Projected systematic uncertainties on the $R_{Cu} - R_D$ extraction as a function of $x$ at all proposed central kinematics. Similar extractions will be performed for $R_{Be} - R_D$, $R_C - R_D$, $R_{Ag} - R_D$ and $R_{Au} - R_D$. Measurements on Iron and gold from SLAC E140 are also shown in black symbols.

In Figure 20 we show the projected uncertainties of our proposed $R_p$ measurements assuming that we will achieve the same accuracy in cross section extractions as the 6 GeV Rosenbluth LT experiments. We also show for comparison the data from E140x (SLAC) [3], and from E99118 (JLab) [32], the only true Rosenbluth LT extractions on proton currently available in the kinematic range we study. A fit of $R$ from R1998 [33] and M.E. Christy model [23] are shown together with theoretical calculations (from PDF fits) from HKN07 [17] and EPS09 [18]. As it can be seen, presently there are very few constraints on these parametrizations from Rosenbluth LT measurements. Our projections for the proton target measurements are also shown in Figure 21 as a function of $x$ together with world DIS data. A similar extraction of $R$ will be performed for the nuclear targets deuterium, beryllium, carbon, copper, silver and gold.

In Figure 22 we show the projected uncertainties on the extraction of $R_{Cu} - R_D$ at all the proposed central kinematics. Parametrizations from HKN07 and EPS09 are also shown for an Iron target together with extractions of $R_{Fe} - R_D$ from the SLAC experiment E140 [1]. Additionally, an extraction of $R_{Fe} - R_D$ from re-analyzed SLAC data by Solvignon and collaborators [7] is displayed at $x = 0.5$ together with the uncertainty in their extraction as a band (Solvignon and collaborators have applied Coulomb corrections to the E140 SLAC data and re-exetracted $R_{Fe} - R_D$). Similarly in Figure 23 we show the projected uncertainties on the extraction of $R_{Cu} - R_D$ at all proposed central kinematics as a function of $x$ together with the E140 measurements on Iron ang gold. From Figures 20, 21, 22 and 23 it can be seen that our projected uncertainties are comparable or better than those of the few measurements from SLAC. We will map the antishadowing region and part of the EMC effect region in great detail with unprecedented accuracy and we will set the most precise limit to date on the possible nuclear dependence of $R$.

## IV. COLLABORATION COMMITMENT TO THE HALL C 12 GEV UPGRADE

The collaboration has a strong commitment to support the equipment for Hall C at 12 GeV.

Hampton University played a leading role in the 6 GeV LT experiments in Hall C, which required many precision systematic studies. These studies led to the detailed understandings of the HMS spectrometer and benefited the Hall C program as a whole. These studies should be repeated for the SHMS spectrometer. Hampton University lead by E.

Christy is responsible for the construction of the drift chambers for the SHMS spectrometer. The design of the drift chambers is complete and construction is in progress. Further commitments include the installation of the chambers into the detector hut and commissioning.

As Hall C staff, David Gaskell will support the SHMS construction and detector assembly and is responsible for ensuring functionality of the Hall C Moller and Compton polarimeters at 12 GeV. He will also update and maintain the Hall C simulation package SIMC, which will help with the spectrometer optics calculations. As Hall C staff, Patricia Solvignon will support Hall C experiments and participate in the SHMS construction. She will be in charge of the implementation of the Polarized $^3$He target in Hall C. As Hall C postdoctoral fellow Simona Malace will support the Hall C physics program and participate in hardware tests for the Hall C 12 GeV upgrade. The James Madison University group lead by I. Niculescu and G. Niculescu are in charge of the construction of the scintillator detectors for SHMS.

## V. SUMMARY

We propose to measure in Hall C at Jefferson Lab with unprecedented statistical precision inclusive inelastic electron-nucleon and electron-nucleus scattering cross sections in the Deep Inelastic Scattering regime spanning a four-momentum transfer range of $1 < Q^2 < 5\ GeV^2$ and a Bjorken $x$ range of $0.1 < x < 0.6$ using hydrogen, deuterium, beryllium, carbon, copper, silver and gold targets to perform high-precision Rosenbluth separations to extract the ratio $R = \sigma_L/\sigma_T$, $R_A - R_D$, and the transverse $F_1$, longitudinal $F_L$, and $F_2$ structure functions in a model-independent fashion.

A recently published study looked at implications of a possible nuclear dependence of $R$ for the antishadowing region. It highlighted the lack of true Rosenbluth precision measurements of $R_A - R_D$ and it showed that even a small difference in $R_A - R_D$ currently allowed within the large uncertainties of the available data could have a big impact on the interpretation of the cross section ratio enhancement in the antishadowing region: the effect could be predominantly due to the contribution of the longitudinal structure function $F_L$, instead of $F_1$ as implicitly asummed in most phenomenological analyses and global nuclear parton distribution fits. Another recent study focused in the EMC effect region re-analyzed SLAC E140 data at $x = 0.5$ including Coulomb corrections and extracted a non-zero value for $R_A - R_D$. That $R_A - R_D$ may be different than zero could have profound implications for our understanding of the origins of both antishadowing and the nucleus EMC effect. We ask for 35 days to set the most precise limit to date on the possible nuclear modifications of $R$.

## VI. APPENDIX

| Quantity | Uncertainty | $d\sigma_{DIS}/\sigma_{DIS}$ pt-pt |
|---|---|---|
| Beam Energy | 0.04% | 0.1% |
| Beam Charge | 0.2 $\mu$ A | 0.5 (*40/I )% |
| Scattered Electron Energy | 0.04% | <0.1 % |
| Electronic Dead Time | 0.25% | 0.25% |
| Computer Dead Time | 0.2% | 0.2% |
| Tracking Efficiency | 0.3% | 0.3% |
| Detector Efficiency | 0.2% | 0.2% |
| Charge Symmetric Background | 0.4% | 0.4% |
| Acceptance | 0.6% | 0.6% |
| Scattered Electron Angle | 0.5 mr | 1.0 (*5.5/$\theta$) % |
| Cryogenic Target Density | 0.1% | 0.1% |
| Cryogenic Target length | 0.1% | 0.1% |
| Cryogenic Target Background | 0.3% | 0.3% |
| Radiative Correction | 1% | 1% [a] |
| Total in Cryogenic Rosenbluth Separation | 1.8%(1.5% at $\theta > 11.0$) | |
| Total in Nuclear Rosenbluth Separation | 1.7% | |
| Total in Nuclear/Cryogenic Ratio | 1.1% | |

[a] It can be bigger for some kinematics.

TABLE X: Point-to-Point systematic uncertainties in the DIS cross section due to the uncertainty in various experimental quantities.

---

[1] S. Dasu *et al.*, Phys. Rev. D **49**, 5641 (1994).
[2] M. N. Rosenbluth, Phys. Rev. **79**, 615 (1956).
[3] L.H. Tao *et al.*, Z. Phys. C **70**, 387 (1996).
[4] A. Airapetian *et al*, Phys. Lett. B **567**, 339-346 (2003).
[5] M. Arneodo *et al.*, Nucl. Phys. B **481**, 23 (1996).
[6] P. Amaudruz *et al.*, Phys. Lett. B **294**, 120 (1992).
[7] P. Solvignon, D. Gaskell, J. Arrington, arXiv:0906.0512 [nucl-exp] (2009).
[8] V. Mamyan, Ph.D. Thesis, University of Virginia, 2010 (arXiv:1202.1457).
[9] A.C. Benvenuti *et al.*, Phys. Lett. B **189**, 483 (1987).
[10] J. Gomez *et al.*, Phys. Rev. D **49**, 4348 (1994).
[11] J. Ashman *et al.*, Z. Phys. C **57**, 211 (1993).
[12] D.M. Alde *et al.*, Phys. Rev. Lett. **64**, 2479 (1990).
[13] Fermi Lab Proposal, http://projects-docdb.fnal.gov/cgi-bin/ShowDocument?docid=395
[14] S. Dasu *et al.*, Phys. Rev. Lett. **60**, 2591 (1988).
[15] V. Guzey *et al.*, Phys. Rev. C **86**, 045201 (2012).
[16] I. Shienbein *et al.*, Phys. Rev. D **77**, 054013 (2008).
[17] M. Hirai, S. Kumano, T.-H. Nagai, Phys. Rev. C **76**, 065207 (2007).
[18] K.J. Eskola, H. Paukkunen, C.A. Salgado, JHEP **0904**, 065 (2004).
[19] L. B. Weinstein, E. Piasetzky, D. W. Higinbotham, J. Gomez, O. Hen and R. Shneor, Phys. Rev. Lett. **106**, 052301 (2011).
[20] O. Hen, E. Piasetzky and L. B. Weinstein, Phys. Rev. C **85**, 047301 (2012).
[21] J. Arrington, A. Daniel, D. Day, N. Fomin, D. Gaskell and P. Solvignon, Phys. Rev. C **86**, 065204 (2012).
[22] J. Seely *et al.*, Phys. Rev. Lett. **103**, 202301 (2009).
[23] M.E. Christy *et al.*, Phys. Rev. C **81**, 055213 (2010).
[24] P.E. Bosted and V. Mamyan, arXiv:1203.2262 [nucl-th].
[25] A. Daniel, Ph.D. Thesis, University of Huston, 2007.
[26] P.E. Bosted, CLAS-NOTE-2004-005, 2004.
[27] D.E. Wiser, Ph.D. Thesis, University of Wisconsin, 1977.
[28] L.W. Mo, Y.S. Tsai, Rev. Mod. Phys. **41**, 205 (1969).

[29] S.P. Malace, Ph.D. Thesis, Hampton University 2006.
[30] A. Aste, C. von Arx, D. Trautmann, Eur. Phys. J. **A26**, 167-178 (2005).
[31] Y. Liang, Ph.D. Thesis, Amercan University, 2002.
[32] V. Tvaskis, Ph.D. Vrije University, 2004.
[33] K. Abe *et al.*, Phys. Lett. B **452**, 194-200 (1999).